

**Local axonal morphology guides the topography  
of interneuron myelination in mouse and human neocortex**

J. Stedehouder<sup>1</sup>, D. Brizee<sup>1</sup>, J. A. Slotman<sup>2</sup>, M. Pascual-García<sup>1</sup>, M. L. Leyrer<sup>3</sup>,  
B. L. J. Bouwen<sup>4,5</sup>, C. M. F. Dirven<sup>5</sup>, Z. Gao<sup>4</sup>, D. M. Berson<sup>3</sup>,  
A. B. Houtsmuller<sup>2</sup>, S. A. Kushner<sup>1</sup>

<sup>1</sup> Department of Psychiatry, Erasmus MC University Medical Center, Rotterdam,  
The Netherlands

<sup>2</sup> Erasmus Optical Imaging Center, Department of Pathology, Erasmus MC  
University Medical Center, Rotterdam, The Netherlands

<sup>3</sup> Department of Neuroscience, Brown University, Providence, Rhode Island, USA

<sup>4</sup> Department of Neuroscience, Erasmus MC University Medical Center,  
Rotterdam, The Netherlands

<sup>5</sup> Department of Neurosurgery, Erasmus MC University Medical Center,  
Rotterdam, The Netherlands

Correspondence to: S.A.K. (s.kushner@erasmusmc.nl)

Word Count: Abstract: 150 words

Manuscript: 4527 words

Display Items: Total 24 (9 Main Figures, 11 Figure Supplements,  
3 Supplementary Tables, 1 Video)

**ABSTRACT**

**GABAergic fast-spiking parvalbumin-positive (PV) interneurons are frequently myelinated in the cerebral cortex. However, the factors governing the topography of cortical interneuron myelination remain incompletely understood. Here, we report that segmental myelination along neocortical interneuron axons is strongly predicted by the joint combination of interbranch distance and local axon caliber. Enlargement of PV+ interneurons increased axonal myelination, while reduced cell size led to decreased myelination. Next, we considered regular-spiking SOM+ cells, which normally have relatively shorter interbranch distances and thinner axon diameters than PV+ cells, and are rarely myelinated. Consistent with the importance of axonal morphology for guiding interneuron myelination, enlargement of SOM+ cell size dramatically increased the frequency of myelinated axonal segments. Lastly, we confirm that these findings also extend to human neocortex by quantifying interneuron axonal myelination from ex vivo surgical tissue. Together, these findings establish a predictive model of neocortical GABAergic interneuron myelination determined by local axonal morphology.**



## INTRODUCTION

Myelination is the insulating ensheathment of axons by oligodendrocytes to enhance action potential propagation and provide metabolic support.<sup>1</sup> Recent studies have shown that a large fraction of neocortical myelination arises from axons of fast-spiking, parvalbumin-positive (PV) interneurons.<sup>2,3</sup> Nearly every cortical PV+ interneuron is myelinated, and most frequently with a proximally-biased axonal topography consisting of short internodes interspersed with branch points.<sup>3,4</sup> In contrast, other neocortical GABAergic interneuron subtypes are more rarely and sparsely myelinated, raising the question of what factors determine this cell type-restricted pattern of neocortical interneuron myelination.

Axonal diameter has been previously demonstrated as an important neuronal factor influencing myelination. In the peripheral nervous system (PNS), a critical threshold of axonal diameter of  $\sim 1\ \mu\text{m}$  has been identified, which largely predicts myelination.<sup>5</sup> However in the central nervous system (CNS), the pattern is much less clear. Axons with diameters  $\sim 200\ \text{nm}$  can become myelinated<sup>6</sup>, while axon diameters as large as  $\sim 800\ \text{nm}$  can remain unmyelinated.<sup>6</sup> *In vitro*, oligodendrocytes reliably initiate myelination of synthetic nanofibers above a critical diameter of  $\sim 300\ \text{nm}$  but rarely do so for smaller diameters.<sup>7-9</sup> The diameter findings appear to extend to grey matter *in vivo*, where myelinated axons  $< 300\ \text{nm}$  are rarely observed.<sup>2,9</sup> Moreover, following acute demyelination regenerated myelin sheaths often re-establish their pre-morbid pattern of myelination, suggesting that intrinsic axonal factors are primary determinants of myelination.<sup>10</sup> Furthermore, oligodendrocytes appear to sense axonal diameters *in vitro*, and adjust their internode length

70 based on fiber diameter.<sup>8</sup> Taken together, axonal diameter is firmly established  
71 as an important determinant underlying internode formation. However, in  
72 contrast to its high predictive validity in the PNS, axonal diameter is only  
73 moderately predictive of myelination topography in the CNS.

74 Here we examine the relationship between cortical interneuron  
75 myelination and axonal morphology in adult mouse prefrontal cortex. We find  
76 that the topography of myelination along individual PV+ axons is strongly  
77 predicted by the joint combination of axonal diameter and interbranch distance.  
78 The bivariate model combining axonal diameter and interbranch distance was  
79 superior to univariate models involving either axonal diameter or interbranch  
80 distance alone. We further explored the model robustness by implementing  
81 bidirectional manipulations of PV+ interneuron size. Enlargement of PV+  
82 interneuron size resulting from cell-type specific deletion of *Tsc1* increased the  
83 incidence of myelinated segments. Conversely, reduction of PV+ interneuron size  
84 by cell-type specific deletion of *Ube3a* decreased the frequency of myelinated  
85 segments. Yet notably, in both cases, the joint combination of interbranch  
86 distance and local axon caliber remained highly predictive of myelin topography.  
87 Lastly, we considered regular-spiking SOM+ cells, which normally have relatively  
88 shorter interbranch distances and thinner axon diameters than PV+ cells, and  
89 are rarely myelinated. However, enlargement of SOM+ cell size by cell type-  
90 specific deletion of *Tsc1* dramatically increased the frequency of myelinated  
91 axonal segments and with a topography accurately predicted by the bivariate  
92 model. Lastly, we find that interneurons reconstructed from human *ex vivo*  
93 surgical tissue also exhibit similar rules governing their axonal myelination.  
94 Together, these results establish a highly predictive model of neocortical

GABAergic interneuron myelination topography based on local axonal morphology.

## RESULTS

### Super-resolution imaging of individual fast-spiking, PV+ interneuron axons

To examine the relationship between the axonal morphology of PV+ interneurons and their myelination, we targeted fluorescent PV+ interneurons in the adult medial prefrontal cortex (mPFC) of *Pvalb::cre<sup>11</sup>;Ai14<sup>12</sup>* mice for whole-cell patch-clamp recording and biocytin filling ( $n = 8$  cells; **Fig. 1a,b; Supplementary Table 1**). Recorded cells exhibited the fast-spiking pattern associated with PV+ interneurons (**Fig. 1c**). Biocytin-labeled cells were imaged by confocal microscopy for reconstruction (**Fig. 1d**), followed by structured illumination microscopy (SIM) for high-resolution analysis of individual axonal segments<sup>13</sup> (see **Methods; Fig. 1-Figure Supplements 1-3**). We systematically analyzed PV+ interneuron axonal segments up to the 7<sup>th</sup> branch order, beyond which myelination was rarely observed in this region.<sup>3,4</sup> Axon shaft diameter averaged  $0.34 \pm 0.01 \mu\text{m}$  (range  $0.16 - 0.98 \mu\text{m}$ ) and decreased with increasing branch order (**Fig. 1e-g**). *En passant* boutons, located primarily on more distal branches ( $\geq 5^{\text{th}}$  branch order), averaged  $0.71 \pm 0.01 \mu\text{m}$  in diameter (range  $0.34 - 1.26 \mu\text{m}$ ; **Fig. 1h**).

### PV+ interneuron myelination co-varies with axon morphology

Myelin was visualized by immunolabeling for myelin basic protein (MBP). Consistent with previous studies<sup>3,4</sup>, reconstructed PV+ interneurons consistently exhibited myelination of their proximal axons (8 out of 8; 100%, **Fig 2a,c**), while

distal axonal segments remained unmyelinated (**Fig. 2b,c**). Myelination of PV+ interneurons typically extended from branch point to branch point (**Fig. 2c**), in which ~84% of myelinated internodes had their boundaries within 5  $\mu\text{m}$  of an axonal branch point (**Fig. 2d**). For each reconstructed interbranch segment, we examined the relationship between the probability of segmental myelination and the average axon shaft diameter using receiver operating characteristic (ROC) analysis.<sup>14</sup> Axon shaft diameter strongly co-varied with myelination, with a critical univariate threshold at 334 nm (area under curve, AUC = 0.93; sensitivity = 97.2%, specificity = 84.4%), above which internodes were often present and below which myelination was rarely observed (**Fig. 2e-g**). However, 30% of interbranch segments with axon shaft diameter >334 nm remained incorrectly classified by the univariate ROC model (15 of 50 segments), suggesting additional deterministic factors underlying the variance in segmental myelination.

We next considered the univariate relationship of interbranch distance with segmental myelination. We found that myelination occurred more frequently along uninterrupted interbranch segments greater than 17.4  $\mu\text{m}$  (AUC = 0.79; sensitivity = 97.2%, specificity = 60.4%; **Fig. 2f,g**). However, similar to the relationship with axonal diameter, a substantial proportion of interbranch segments >17.4  $\mu\text{m}$  were unmyelinated (48%, 35 of 73 segments).

Therefore, we implemented a bivariate ROC analysis<sup>15</sup> to explore whether the intersection of interbranch distance and axonal diameter might yield improved estimates of segmental myelination. Using a bivariate ROC analysis, the optimal interbranch distance and axonal diameter were 13.7  $\mu\text{m}$  and 334 nm, respectively (AUC = 0.99; **Fig. 2f,g**). The joint combination of these two

thresholds correctly predicted whether 128 of 132 segments contained an internode (97.0% accuracy), a significant improvement over the univariate models (interbranch distance: 70.5% accuracy, Fisher's Exact Test  $P < 0.001$ ; axonal diameter: 87.9% accuracy, Fisher's Exact Test  $P = 0.005$ ). In particular, the bivariate model correctly predicted 35 of 36 myelinated internodes (sensitivity = 97.2%), matching that of the univariate predictors (Fisher's Exact Test  $P = 0.99$ ). However, the joint combination of interbranch distance and axonal diameter also predicted with high accuracy those segments in which myelination was absent (93 of 96 segments, specificity = 96.9%), in contrast to the univariate models (Fisher's Exact Test; axonal diameter:  $P = 0.004$ , interbranch distance:  $P < 0.001$ ). These findings suggest that the combination of interbranch distance and axonal diameter are highly predictive of segmental myelination along PV+ interneurons.

To independently corroborate the findings from supra-resolution imaging, we utilized electron microscopy (EM) for assessing the morphology and myelination of PV+ cell axons. We utilized a genetic labeling method to enhance the electron dense contrast of PV+ cell axons by stereotactic injection of a cre-dependent adeno-associated virus (AAV2) into the mPFC of *Pvalb::cre* mice. Virus-transduced *Pvalb::cre*+ cells expressed the EM marker APEX2<sup>16</sup> fused with membrane-targeted GFP (mGFP-APEX2), permitting cell-type specific visualization of labeled PV+ cells in both fluorescence and electron micrographs (**Fig. 3a-c,e,f**). Prior to ultrastructural analysis, we used confocal microscopy to confirm that GFP+ neurons resembled PV+ cells morphologically. We also confirmed that nearly all of the virally labeled cells were immunopositive for PV ( $93.9 \pm 1.3\%$ ; **Fig. 3b-d**). We then used APEX2-mediated peroxidase

histochemistry to produce intracellular electron dense labeling. PV+ cells were readily detected by their darkened cytoplasmic staining in electron micrographs. This allowed us to identify axonal processes belonging to PV+ interneurons, whether myelinated or not (**Fig. 3e,f**). The distributions of axon shaft diameter and bouton diameter, and their relationship with axonal branch order, were also highly comparable to previous ultrastructural analyses of fast-spiking, PV+ interneurons.<sup>16,17,18</sup> Consistent with the fluorescence microscopy analysis (**Fig. 2**), myelination was observed exclusively around PV+ axonal fibers with shaft diameters >330 nm. Mean diameter was significantly larger in myelinated than in unmyelinated segments (**Fig. 3g**). Thus, axon morphology strongly predicts myelination of PV+ interneurons using two independent methods.

## **Bi-directional manipulation of PV+ axon morphology alters myelination**

In order to examine the robustness of axonal morphology in predicting PV+ interneuron myelination topography, we performed cell-type specific manipulations known to influence axonal geometry. Deletion of the *Tsc1* gene has been previously shown to induce enlarged somata of various neuronal cell types across a diversity of brain regions.<sup>19-22</sup> Moreover, the Akt-mTOR pathway, a downstream target of *Tsc1*, is one of the main regulators of axon caliber.<sup>23</sup> Conversely, mice harboring a deletion of *Ube3a* have recently been shown to exhibit smaller neurons<sup>24,25</sup> with reduced axonal diameters in corpus callosum.<sup>26</sup>

To obtain PV cell-specific deletions, *Pvalb::cre* mice were crossed with floxed *Tsc1*<sup>*f/f*</sup> mice (PV::TSC1) and floxed *Ube3a*<sup>*p/f*</sup> mice (PV::UBE3A) (**Fig. 4a; Fig. 4-Figure Supplements 1-2**). PV+ cells in adult mPFC of PV::TSC1 mice exhibited a ~50% increase in soma size, in accordance with a strong

upregulation of pS6<sup>235/236</sup>, a downstream target of mTOR (**Fig. 4b,c**). PV::TSC1 cells showed filopodia-like extensions on their soma and proximal dendrite, which were not observed in PV::WT cells (**Fig. 4-Figure Supplement 1f**). Conversely, PV::UBE3A mice exhibited a ~15% reduction in PV+ interneuron soma area (**Fig. 4b,c**). Notably, mPFC PV cell density was similar across PV::UBE3A, PV::TSC1, and PV::WT mice (**Fig. 4-Figure Supplement 3a-b**).

To examine axon caliber, adult PV::TSC1, PV::UBE3A and PV::WT mice received unilateral stereotactic injections in the mPFC of adeno-associated virus (AAV) containing cre-dependent GFP. Fourteen days later, mice were sacrificed and axons originating from GFP+ somata were imaged using SIM (**Fig. 4d**). Since we observed that the diameter of the 1<sup>st</sup> branch order strongly correlated to diameter of consecutive axonal segments (Fig. 1), we measured primary axonal diameter at the 1<sup>st</sup> branch order for GFP-labelled cells from PV::TSC1, PV::UBE3A and PV::WT cells as a high-throughput indication of axon caliber. Consistent with enlarged somata, this analysis revealed a significantly increased primary axonal caliber of PV::TSC1 PV+ cells compared to PV::WT cells (**Fig. 4e,f**). In contrast, axons from PV::UBE3A showed a non-significant trend toward decreased primary axon caliber compared to PV::WT cells (**Fig. 4e,f**).

We next performed whole-cell electrophysiological recordings of adult mPFC PV+ cells combined with biocytin-filling and *post hoc* MBP immunofluorescence as previously described (**Fig. 5a; Fig. 4-Figure Supplement 4**).<sup>3,4</sup> Recorded PV+ cells in PV::TSC1, PV::UBE3A and PV::WT exhibited fast-spiking firing characteristics, with no detectable differences between genotypes (**Fig. 5b-d; Fig. 4-Figure Supplement 4**). Confocal imaging followed by proximal axonal reconstructions (**Fig. 5e-h**) revealed that all

220 PV::TSC1 cells exhibited axonal myelination (13 of 13 cells; 100%; **Fig. 5f-i**),  
221 similar to PV::WT cells (10 of 11 cells; 90%) and PV::UBE3A cells (7 of 8 cells;  
222 88%). *Tsc1*-deficient PV+ cells showed increased axonal myelination per cell  
223 compared to PV::WT cells (**Fig. 5j**). Interestingly, the increase in myelination per  
224 cell was associated with both an increase of average internode length (**Fig. 5k**)  
225 as well as a higher number of internodes per cell (**Fig. 5l**), but without a change  
226 of interbranch distance (**Fig. 5m**). Onset of myelination, measured as axonal  
227 distance from the soma or originating dendrite to the beginning of the first  
228 internode, was unchanged (**Fig. 5n**). In contrast to PV::TSC1 cells, *Ube3a*-  
229 deficient PV+ cells exhibited a decrease in axonal myelination (**Fig. 5i,j**),  
230 including both a lower number and shorter length of internodes (**Fig. 5k,l**),  
231 consistent with their reduced soma size. Finally, the initial point of myelin onset  
232 from the soma was unchanged in PV::UBE3A cells (**Fig. 5n**). Despite these PV cell  
233 type-specific alterations in myelination, no robust changes were observed in  
234 global myelination (**Fig. 5-Figure Supplement 1a,b**) or CC1+ mature  
235 oligodendrocyte density (**Fig. 5-Figure Supplement 1c,d**).

236       Systematic analysis of individual PV+ interneuron axonal segments in  
237 PV::UBE3A and PV::TSC1 cells confirmed a similarly strong co-variation between  
238 axon morphology and segmental myelination as observed in PV::WT mice (**Fig.**  
239 **5o-s**). ROC analysis of PV::UBE3A cells yielded bivariate thresholds of axonal  
240 diameter > 332 nm and interbranch distance > 14.1  $\mu$ m (sensitivity = 100%,  
241 specificity = 97.5%; AUC = 0.99) (**Fig. 5p,q**). Analogously, ROC analysis of the  
242 PV::TSC1 cells yielded bivariate thresholds of axonal diameter > 378 nm and  
243 interbranch distance > 18.6  $\mu$ m (sensitivity = 100%, specificity = 94.6%; AUC =  
244 0.99) (**Fig. 5r,s**). Similar to PV::WT, the bivariate model for PV::TSC1



significantly improved the prediction accuracy of segmental myelination compared to the univariate models (axonal diameter:  $P = 0.015$ ; interbranch distance:  $P = 0.027$ ). For PV::UBE3A, the bivariate model was a significant improvement over the univariate model based on interbranch distance ( $P = 0.004$ ), but statistically similar to the univariate model for axonal diameter ( $P = 0.500$ ). Together, these findings demonstrate the robustness of the joint combination of interbranch distance and axonal diameter for accurately predicting the topography of PV+ interneuron myelination *in vivo*, across a wide range of axonal morphologies.

#### **SOM+ and PV+ interneurons adhere to similar myelination rules**

Regular spiking, SOM+ interneurons<sup>27</sup> have relatively few myelinated internodes along their axons in mPFC<sup>3</sup> and contribute minimally to total neocortical myelination content.<sup>2</sup> Is this sparse myelination also predicted by their axonal morphology, as we observed for PV+ interneurons? Do SOM+ interneuron axons share the thinner shaft diameters or more closely spaced branch points of unmyelinated segments of PV+ axons?

To examine this possibility, we performed whole-cell recordings and intracellular biocytin-labeling of SOM+ interneurons in mPFC using *Sst::cre*<sup>28</sup>, *Ai14*<sup>12</sup> mice ( $n = 10$ ; **Fig. 6a-d; Fig. 1-Figure Supplement 3**). The identity of filled cells was further confirmed as SOM+ interneurons based upon their characteristic electrophysiological and morphological features<sup>27</sup> (**Fig. 6c,d; Supplementary Table 2; Fig. 7-Figure Supplement 1e**). Among the 10 reconstructed SOM+ axons, we found only a single myelinated internode (**Fig. 6e-h**). Axonal shaft diameter as quantified using SIM averaged  $0.303 \pm 0.015 \mu\text{m}$

(range 0.222 - 0.561  $\mu\text{m}$ ; **Fig. 6f**, **Fig. 7-Figure Supplement 1f**) and decreased with increasing branch order (**Fig. 6g**). Notably, the vast majority of unmyelinated SOM+ axonal segments had smaller diameters and/or more closely spaced branch points than the threshold values identified among myelinated segments in PV+ interneurons (**Fig. 6h** inset; dashed line).

Since we identified only a single myelinated segment, we could not reliably determine critical thresholds for axonal diameter and interbranch distance thresholds among wild-type SOM+ interneurons. Notably, however, this single myelinated segment had an axonal diameter of 561 nm and interbranch distance of 16.8  $\mu\text{m}$ , which exceeded the morphometric thresholds we identified for wildtype PV+ interneurons. Similarly, the vast majority of unmyelinated SOM+ interneuron axon segments fell below morphometric thresholds for axonal diameter and/or interbranch distance identified for PV::WT cells (79 of 88 segments; 89.8%) (**Fig. 6h**). These data indicate that the myelination rules derived from the analysis of PV+ cells may be generalizable to other neocortical interneurons, including SOM+ cells.

### **Genetic manipulation of SOM+ axon morphology induces *de novo* myelination.**

Factors other than axon morphology could explain why SOM+ interneurons are largely unmyelinated, such as expression of active inhibitors of myelination.<sup>29</sup> We therefore asked whether we could induce *de novo* myelination of SOM+ cells by altering their axonal morphology. Using an analogous approach to that we used for PV+ cells, we deleted *Tsc1* specifically in SOM+ cells by crossing *Sst::cre* and floxed *Tsc1*<sup>*fl/fl*</sup> mice. SOM+ interneurons identified by *post*

*hoc* immunolabeling had ~65% larger soma size in mPFC compared to WT mice (Fig. 7a,b; Fig. 7-Figure Supplement 1). Moreover, cre-dependent viral labeling of SOM+ cells followed by SIM imaging showed increased axon calibers for SOM::TSC1 cells (1<sup>st</sup> order branches) compared to WT mice (Fig. 7c,d). SOM+ cell density was unchanged in the mPFC of SOM::TSC1 mice (Fig. 7-Figure Supplement 2a,b).

We next performed whole-cell electrophysiological recordings in mPFC SOM+ cells combined with biocytin-filling and *post hoc* MBP immunofluorescence to examine the influence of the enlarged morphology on axonal myelination (Fig. 7e,f; Fig. 1-Figure Supplement 3; Fig. 7-Figure Supplement 1). Recorded SOM::TSC1 cells exhibited reduced input resistance and intrinsic excitability, with no changes in single action potential characteristics (Fig. 7-Figure Supplement 3).

Confocal microscopy followed by axonal reconstruction showed that whereas SOM::WT cells were rarely myelinated (0 out of 6; 0%), which is in line with the *Sst::cre,Ai14* cells, myelination of SOM::TSC1 cells was highly frequent (11 out of 11; 100%; Fig. 7f-h). Moreover, SOM::TSC1 cells showed corresponding increases in total length of myelination (Fig. 7i), internode length (Fig. 7k), and number of internodes (Fig. 7j). Myelin onset appeared at  $55.8 \pm 7.2 \mu\text{m}$  from the soma (Fig. 7n), typically initiating between the 2<sup>nd</sup> and 6<sup>th</sup> branch order. No myelin was identified on more distal axonal segments (branch order  $\geq 10$ ). Myelination was found equally on the primary axon and on axon collateral branches (Fig. 7l). Furthermore, SOM::TSC1 myelination was constrained by axonal branch points, in that 87% of internodes began or ended within  $5 \mu\text{m}$  of a branch point (Fig. 7m).

Analyses of individual axonal segments using SIM along SOM::TSC1 cells revealed a similar relationship between myelination and the joint combination of axonal diameter and interbranch distance (**Fig. 7o-q**) as found in wildtype PV+ cells (**Fig. 2f, Fig. 5n,o**). ROC analysis of SOM::TSC1 cells yielded thresholds of axonal diameter > 406 nm and interbranch distance > 11.8  $\mu$ m (sensitivity = 0.95, specificity = 0.90; AUC = 0.94) (**Fig. 7p**). The bivariate model exhibited a significantly improved the prediction accuracy for segmental myelination compared to the univariate models (axonal diameter:  $P < 0.001$ , interbranch distance:  $P < 0.001$ ). These findings suggest that axonal morphology, and in particular the combination of axonal caliber and interbranch distance, governs the local segmental myelination of PV+ and SOM+ neocortical interneurons.

Neocortical SOM+ interneurons are morphologically and electrophysiologically heterogeneous.<sup>30</sup> Therefore, to further examine the extent of SOM::TSC1 myelination across a wider population of cells, we employed SOM-specific sparse viral transduction using cre-dependent GFP expression in adult mPFC, followed by MBP immunofluorescence (**Fig. 8a**). Although this method precludes electrophysiological confirmation of adapting spiking patterns and detailed axonal reconstructions, it provides a higher-throughput examination of mPFC SOM+ interneuron myelination. We examined axons originating from mPFC layer II-V GFP+ interneuron somata from SOM::WT and SOM::TSC1 mice for colocalization with MBP (**Fig. 8b**). Of 26 SOM::WT+ cells examined, 4 (15%) were myelinated (**Fig. 8c**). Conversely, of 50 SOM::TSC1+ cells examined, 46 (92%) were myelinated ( $P < 0.001$ ; **Fig. 8c**). Consistent with the high proportion of SOM+ cell myelination, the mPFC of SOM::TSC1 exhibited a marked increase of

global myelination (**Fig. 8d,e**) and a higher density of CC1+ mature oligodendrocytes (**Fig. 8f,g**).

Together, these data suggest that axonal morphology is necessary and sufficient to govern neocortical interneuron myelination. In particular, we propose that the combination of interbranch distance and axonal diameter together determine the topographical distribution of internodes along the axons of neocortical interneurons.

### **Human neocortical interneurons adhere to similar myelination rules**

We next examined whether the above findings in mice also extend to human neocortex. Using *ex vivo* resected tissue from patients undergoing tumor surgery, we performed whole-cell electrophysiological recordings (**Supplementary Table 3**) and intracellular biocytin labeling with *post hoc* MBP immunofluorescence of fast-spiking interneurons classified on the basis of morphology and electrophysiology (**Fig. 9a-e**; 4 cells from 4 donors; see **Methods**).

Reconstructed human fast-spiking interneurons exhibited a similar total length of myelination ( $432.0 \pm 137.9 \mu\text{m}$ ), average internode length ( $44.7 \pm 4.9 \mu\text{m}$ ), and number of internodes ( $9.7 \pm 1.9$  internodes) as previously described.<sup>3</sup> Myelin onset appeared at  $36.2 \pm 13.3 \mu\text{m}$  from the soma, initiating between the 1<sup>st</sup> (2 out of 4 cells; 50%) and 3<sup>rd</sup> branch order (2 out of 4 cells; 50%). Analogous to mouse interneurons, no myelin was identified on more distal axonal segments (branch order  $\geq 10$ ; **Fig. 9f**).

Analyses of individual axonal segments using SIM along human fast-spiking interneurons revealed a similar relationship between myelination and

the joint combination of axonal diameter and interbranch distance (**Fig. 9h-j**) as found in mouse PV+ cells (**Fig. 2f**). ROC analysis of human interneurons yielded thresholds of axonal diameter > 328 nm and interbranch distance > 13.7  $\mu$ m (sensitivity = 92.5%, specificity = 89.3%; AUC = 0.96; **Fig. 9k**). The accuracy of the bivariate model (90.6%, 87 of 96 segments) was significantly higher than interbranch distance (66.7%,  $P < 0.001$ ) but non-significantly different from axonal diameter (83.3%,  $P = 0.198$ ). Together, these findings suggest that mouse and human neocortical interneurons follow similar morphological rules guiding the topography of axonal myelination.

## Discussion

Fast-spiking, PV-positive interneurons are frequently myelinated in the cerebral cortex, and their myelination forms a considerable proportion of cortical myelin.<sup>2,3,31</sup> PV+ myelination exhibits a proximally-biased topography consisting of short internodes interspersed by branch points, whereas more distal axonal segments decorated with frequent *en passant* boutons remain unmyelinated.<sup>3,4</sup> Conversely, other interneuron subclasses, such as irregularly spiking SOM-positive interneurons, are sparsely myelinated and contribute minimally to the total content of neocortical myelin.<sup>3</sup> However, it has remained unknown why PV+ interneurons are preferentially myelinated compared to other neocortical interneuron subtypes. Here, we have provided evidence suggesting that axonal morphology is a strong determinant of the topography of myelination along individual axons.

Using single-cell axonal reconstructions, we revealed a high co-variation between segmental myelination and the joint combination of interbranch

distance ( $\sim 14\ \mu\text{m}$ ) and axonal diameter ( $\sim 330\ \text{nm}$ ) thresholds. These parameters were remarkably similar across two interneuron subtypes (PV vs. SOM) and independent of genetic manipulation of their morphologies. Moreover, our results appear to provide an explanation for the proximally-biased topography of PV+ interneuron myelination, in which internodes are consistently present at the first axonal branch order with a declining probability at increasing branch orders.<sup>3,4</sup> Given that axonal shaft diameter decreases with increasing branch order (see **Fig. 1h**, but also <sup>18</sup>), distal axonal segments would therefore remain unmyelinated by virtue of their thinner axon shafts, despite often retaining supra-threshold interbranch distances. Differences in axon morphology presumably also account, at least in part, for the more robust myelination of neocortical PV+ interneurons relative to other interneuron subtypes.<sup>2,3</sup> However, it remains unknown whether the myelination rules revealed here for interneurons extends to neocortical pyramidal cells, which also exhibit interspersed unmyelinated segments.<sup>32</sup> Prior studies using serial EM have identified a  $\sim 300\ \text{nm}$  threshold of axon diameter for both GABAergic as well as non-GABAergic axons, suggesting the morphological parameters could well extend to excitatory axons.<sup>2</sup>

We find here that an uninterrupted interbranch distance of  $\sim 14\ \mu\text{m}$  is a strict requirement for segmental myelination in both PV+ and SOM+ interneurons. This threshold approximates the length of the smallest myelinated internodes found on neocortical axons of PV+ interneurons<sup>3</sup> and pyramidal neurons<sup>32</sup>, and more generally across unspecified cell types in the cerebral cortex.<sup>33</sup> Notably, pre-myelination nodal clustering – the clustering of voltage-gated sodium channels which later form nodes of Ranvier – exists in similar

intervals.<sup>34</sup> One possibility is that ~14  $\mu$ m is the minimum biophysical length compatible with oligodendrocyte ensheathment.

The functional consequence of cortical interneuron myelination is currently unknown. Fast-spiking PV+ interneurons have demanding metabolic requirements<sup>35</sup>. As myelination has been established to function critically in providing axonal metabolic support<sup>36–38</sup>, myelination of PV+ interneurons could function by helping to optimize axonal energy utilization. Moreover, PV+ interneurons coordinate fast synchronizing network activity in the gamma frequency range<sup>39</sup>, for which segmental interneuron myelination could enhance synchronized inhibition through local modulation of action potential conduction velocity. This is particularly interesting given recent findings that distance-dependent inhibition functions in regulating gamma synchrony.<sup>40</sup>

Only a small fraction of neocortical myelin localizes along the axons of irregular-spiking SOM+ interneurons, even though these cells represent ~30% of interneurons.<sup>41</sup> Accordingly, we found that the limited myelination of SOM+ interneurons was highly consistent with their generally thinner axon diameter and shorter interbranch distances compared to PV+ cells. Enlargement of SOM+ interneurons by cell-type restricted deletion of *Tsc1* led to a dramatic increase in the frequency and extent of axonal myelination. Notably, this *de novo* myelination of SOM::TSC1 cells was also accurately predicted by the same joint axonal diameter and interbranch distance parameters as identified in PV+ interneurons. However, compared to the PV::TSC1 cell manipulation, SOM::TSC1 mice exhibited a more robust increase of global myelination in the mPFC, which was accompanied by an increased number of CC1+ mature oligodendrocytes. One possibility for this finding is that PV+ cell morphology is already largely



optimized for supra-threshold morphology permissive of myelination, in contrast to SOM<sup>+</sup> cells which are predominantly unmyelinated under normal conditions and therefore exhibit a greater magnitude increase of myelination when their morphology is enlarged by deletion of *Tsc1*. A second non-mutually exclusive possibility is that SOM::TSC1 deletion results in additional non-cell autonomous effects that enhance global myelination and recruitment of mature oligodendrocytes.

An important outstanding question is whether the axonal morphology rules of PV<sup>+</sup> and SST<sup>+</sup> interneurons extend to neocortical glutamatergic pyramidal cells.<sup>42</sup> Some evidence exists to suggest that analogous morphological thresholds might also extend to non-GABAergic cells in the neocortex.<sup>2,43</sup> For example, the more frequently myelinated first-order axonal segment of PV<sup>+</sup> GABAergic axons has a ~2.5-fold larger caliber than glutamatergic pyramidal neurons.<sup>44</sup> However, the highly discontinuous topography of internodes along glutamatergic pyramidal cells also suggests a major influence of factors beyond morphology.<sup>45</sup> One possibility is that myelination of pyramidal neurons involves a combination of attractive and/or repulsive molecular cues, such as neuregulin-ErbB signaling<sup>46</sup> or glutamatergic signaling<sup>47-51</sup>, in addition to axonal morphological thresholds.<sup>52</sup> Furthermore, a recent study observed that a subset of neocortical oligodendrocytes exclusively ensheath GABAergic interneurons, raising the possibility that distinct subtypes of oligodendrocytes might have neuronal cell type-specific rules governing axonal myelination.<sup>53</sup>

Myelination of neocortical glutamatergic pyramidal neurons is modulated *in vivo* by experience, as well as direct manipulation of neuronal activity.<sup>54</sup> Activity-dependent myelination also extends to neocortical PV<sup>+</sup> interneurons, a

finding associated with concordant alterations in axonal morphology.<sup>4</sup> When considered together with the current findings, it is therefore possible that neuronal activity-dependent myelination<sup>55,56</sup> in the cerebral cortex might be mediated by axonal morphological plasticity.

The current studies were focused primarily on locally-projecting GABAergic interneurons in prefrontal cortex. However, several studies have identified long-range GABAergic projecting cells including, but not limited to, PV+ and SOM+ subclasses.<sup>57-60</sup> The high proportion of cerebral cortex PV+ cells exhibiting axonal myelination<sup>3</sup> makes it likely that long-range PV+ cells are also myelinated. However, due to technical limitations of slicing and intracellular biocytin labeling, it was not possible to definitively identify and reconstruct long-range GABAergic axons. Thus, the question remains open whether long-range GABAergic axons are also frequently myelinated and whether axonal morphology is similarly predictive of their myelination. Moreover, a related issue regards whether the present findings acquired in grey matter also extend to white matter, especially given regional differences among oligodendrocyte lineage cells.<sup>61,62</sup>

Myelination of GABAergic interneurons has been observed in multiple mammalian species<sup>31</sup>. Notably, human neocortical fast-spiking PV+ interneurons appear to have more extensive total myelination per cell than is observed in mice.<sup>3,43</sup> This raises the possibility that neocortical interneuron myelination might have a crucial influence on higher cognitive function, as well as potentially in the pathophysiology of disorders involving CNS myelination impairments, such as multiple sclerosis or schizophrenia.<sup>31,48</sup> Therefore, it is important to determine the extent to which the morphological determinants of interneuron

myelination are evolutionarily conserved. Here, we have performed axonal reconstructions and determined the topographical distribution of myelin internodes along human fast-spiking interneurons from acutely resected *ex vivo* neocortical tissue. We found that segmental neocortical interneuron myelination conforms to similar bivariate morphological thresholds as observed in mouse neocortex, on the basis of interbranch distance and axonal diameter, suggesting a species conservation of the biophysical constraints on the myelinating function of oligodendrocytes.

In conclusion, we demonstrate that the joint combination of interbranch distance and axonal shaft diameter accurately predicts the topography of neocortical interneuron myelination *in vivo* in both mouse and human.

507 **METHODS**

508 *Mice*

509 All experiments were approved by the Dutch Ethical Committee and in  
510 accordance with the Institutional Animal Care and Use Committee (IACUC)  
511 guidelines. The following mouse lines were obtained from Jackson Laboratory:

512 *Pvalb<sup>tm1(cre)Arbr</sup>/J* mice (*Pvalb::cre*)<sup>11</sup>

513 [www.jax.org/strain/008069](http://www.jax.org/strain/008069)

514 *Sst<sup>tm2.1(cre)Zjh</sup>/J* (*Sst::cre*)<sup>28</sup>

515 [www.jax.org/strain/013044](http://www.jax.org/strain/013044)

516 *Gt(ROSA)26Sor<sup>tm14(CAG-tdTomato)Hze</sup>/J* (Ai14)

517 [www.jax.org/strain/013044](http://www.jax.org/strain/013044)<sup>12</sup>

518 *Tsc1<sup>tm1Djk</sup>/J* (*Tsc1<sup>f/f</sup>*)

519 [www.jax.org/strain/005680](http://www.jax.org/strain/005680)

520 *C57BL/6J* (WT)

521 [www.jax.org/strain/000664](http://www.jax.org/strain/000664)

522 Floxed *Ube3a* mice (*Ube3a<sup>p+/mf</sup>*) were described previously.<sup>63</sup>

523 All lines were backcrossed for more than 10 generations in C57BL/6J.

524 Reporter lines were crossed to obtain heterozygous *Pvalb::cre*/heterozygous

525 Ai14 (*Pvalb::cre*,Ai14) and heterozygous *Sst::cre*/heterozygous Ai14

526 (*Sst::cre*,Ai14). Mutant lines were crossed to obtain heterozygous

527 *Pvalb::cre*/homozygous *Tsc1<sup>f</sup>* (PV::TSC1). Heterozygous

528 *Pvalb::cre*/heterozygous *Ube3a<sup>p+/mf</sup>* (PV::UBE3A) were obtained by crossing male

529 homozygous *Pvalb::cre* with female *Ube3a<sup>p+/mf</sup>*. Heterozygous *Pvalb::cre* mice

530 wildtype littermates for the mutant alleles from both breeding lines were used as

531 controls (PV::WT). Both mutant lines were viable and healthy, although PV::TSC1

mice developed a severe ataxia during development (**Video 1**). We have occasionally observed spontaneous seizures during routine handling in PV::TSC1 but not PV::UBE3A lines. In addition, mutant lines were crossed to obtain heterozygous *Sst::cre*/homozygous *Tsc1<sup>f</sup>* (SOM::TSC1). Heterozygous *Sst::cre* mice wildtype littermates for the mutant alleles from this breeding lines were used as controls (SOM::WT). SOM::TSC1 mice did not display any behavioral abnormalities. No spontaneous seizures were observed during routine handling.

For all experiments, mice were used from 8 to 12 weeks of age. Mice were group-housed and maintained on a 12 h light/dark cycle (lights on 07:00-19:00) with *ad libitum* access to food and water. All experiments were performed during the light phase of the cycle.

#### *Human Brain Tissue*

Infiltrated peri-tumoral neocortical tissue was obtained from 4 patients undergoing tumor resection surgery at the Department of Neurosurgery (Erasmus University Medical Center, Rotterdam, The Netherlands). All procedures regarding human tissue were performed with the approval of the Medical Ethical Committee of the Erasmus University Medical Center. Written informed consent of each patient was provided in accordance with the Helsinki Declaration.

Patient #1 was an 84-year old male who presented with a glioblastoma in the right parieto-occipital lobe. He had no significant psychiatric or past medical history, and no history of epilepsy or seizures. Patient received no anti-epileptic or cytostatic medication.

Patient #2 was a 52-year old male who presented with metastases secondary to a melanoma in right temporal lobe. He had no significant psychiatric or other notable past medical history, and no history of epilepsy or seizures. Patient received no anti-epileptic or cytostatic medication.

Patient #3 was a 62-year old male who presented with a right temporal lobe glioblastoma. He had no history of seizures, or notable psychiatric or medical history. Patient received no anti-epileptic or cytostatic medication.

Patient #4 was a 80-year old male who presented with a glioblastoma in the right frontoparietal lobe. He had no significant psychiatric or other notable past medical history, no history of epilepsy or seizures, and received no anti-epileptic or cytostatic medication.

#### *Viral Labeling and CNO injections*

Adult mouse viral labelling was performed as reported before<sup>3</sup>, with minor adjustments. Specifically, adult PV::TSC1, PV::UBE3A, PV::WT, SOM::TSC1 and SOM::WT were used for axon diameter analysis, electrophysiology and single-cell reconstructions. Uncrossed heterozygous *Pvalb::cre* mice were used for PV-specific electron microscopy using APEX2.

The following viral vectors were used:

AAV9/CAG-Flex-eGFP (University of Pennsylvania Viral Vector Core).

AAV2/CAG-Flex-mGFP-APEX2 (a gift from M. L. Leyrer and D. M. Berson)[

[Leyrer, M. L., Berg, D. J., Briggman, K. L., Berson, D. M. A genetically encoded

marker for light- and electron-microscopic analysis of neuronal cell types.

Program No. 186.12/LLL5. 2016 Neuroscience Meeting Planner. San Diego, CA:

Society for Neuroscience, 2016. Online.]

Anesthesia was induced using 5% isoflurane (O<sub>2</sub> flow of 0.5 L/min), and subsequently maintained with 1-2% isoflurane during surgery. Body temperature was maintained at 37°C. Mice were placed into a custom-made stereotaxic frame using a mouth bar (Stoelting) for head fixation. Analgesia was provided systemically by subcutaneous Temgesic injection (buprenorphine 0.5 mg/kg) and locally by xylocaine spray (100 mg/mL, AstraZeneca) directly applied on the skull. To access the brain, a longitudinal scalp incision of ~1 cm length was made to reveal the skull, and a small craniotomy (<1 mm) was performed overlying the injection sites at the following coordinates (in mm): mPFC: +1.75 bregma, ±0.35 lateral, -1.9 dorsoventral (mm, from brain surface). Mice used for electrophysiological recordings received 0.5 µL in a ¼ dilution in 0.1 M PB. Virus was aspirated in a borosilicate glass micropipette, which was slowly lowered to the target site. Virus injection was controlled by an automated syringe pump (infusion speed 0.1 µl/min). At the conclusion of the injection, the micropipette was maintained in place for 5 min and then slowly withdrawn. The surgical wound was closed with skin-glue (Derma+flex). Mice were left to recover for exactly 14 days to allow expression of the GFP protein. Importantly, mice were single-housed after surgery until used for electrophysiology or perfusion and immunofluorescence processing.

#### *Electrophysiology*

##### *Mice.*

Anesthesia was induced using 5% isoflurane and mice were decapitated in ice-cold, NMDG-based cutting solution containing (in mM): 93 N-methyl-d-glucamine (NMDG), 93 HCl, 30 NaHCO<sub>3</sub>, 25 D-glucose, 20 HEPES, 5 Na-ascorbate,

606 2 thiourea, 10 MgCl<sub>2</sub>, 3 Na-pyruvate, 2.5 KCl, 1.25 NaH<sub>2</sub>PO<sub>4</sub> and 0.5 CaCl<sub>2</sub> (300  
607 mOsm, pH 7.4) oxygenated with 95% O<sub>2</sub>/5% CO<sub>2</sub> before decapitation. After  
608 decapitation, the brain was quickly dissected. Coronal slices from the frontal  
609 cortex (300 µm) were cut with a vibrating slicer (Microm HM 650V, Thermo  
610 Scientific) and incubated in cutting solution at 37 °C for 5 min., followed by  
611 oxygenated (95% O<sub>2</sub>/5% CO<sub>2</sub>) artificial cerebrospinal fluid (aCSF) at 37 °C for 15  
612 min. ACSF contained (in mM) 127 NaCl, 25 NaHCO<sub>3</sub>, 25 D-glucose, 2.5 KCl, 1.25  
613 NaH<sub>2</sub>PO<sub>4</sub>, 1.5 MgSO<sub>4</sub> and 1.6 CaCl<sub>2</sub>. Slices were then allowed to recover at room  
614 temperature in the dark for at least 1 h before recordings.

615 In *Pvalb::cre;Ai14* and *Sst::cre;Ai14* mice, PV<sup>+</sup> and SOM<sup>+</sup> interneurons  
616 respectively were visualized by native tdTomato fluorescence using an RFP filter  
617 (Semrock, Rochester, NY, USA). In PV::TSC1, PV::WT, and PV::UBE3A mice, PV<sup>+</sup>  
618 interneurons were visualized by expression of GFP using a GFP filter (Semrock,  
619 Rochester, NY, USA). Similarly, in SOM::TSC1 and SOM::WT mice, SOM<sup>+</sup>  
620 interneurons were visualized by expression of eGFP using a GFP filter. Whole-  
621 cell recordings were made from layer III-V of the prelimbic area of the mPFC  
622 (between ~200 and 600 µm from midline; see **Fig. 1-Figure Supplement 3**;  
623 bregma: +2.10 till +1.54 mm) at between ~20 µm and ~60 µm of the slice  
624 surface using borosilicate glass pipettes (3.5–5.5 MΩ resistance) with  
625 intracellular solution containing (in mM) 120 K-gluconate, 10 KCl, 10 HEPES, 10  
626 K-phosphocreatine, 4 ATP-Mg, 0.4 GTP, and 5 mg/ml biocytin (pH was adjusted  
627 to 7.4 using KOH, and osmolarity measured 285-290 mOsm).

628 Recordings were performed in aCSF at near-physiological temperatures  
629 (32-33°C) using HEKA EPC10 quattro amplifiers and Patchmaster software (40  
630 Hz sampling rate). Series resistance was typically <25 MΩ and fully compensated



for bridge balance and capacitance; recordings in which the series resistance exceeded 25 M $\Omega$  were not included in the pooled averages. No correction was made for liquid junction potential. Data analysis was performed offline using Igor Pro v6 (Wavemetrics). Individual interneurons were recorded and filled for at least 20 minutes. In addition, cells were injected at least 10 times with large depolarizing currents in current clamp mode (500 pA, 5 Hz, 2 s) to facilitate biotin diffusion into fine axonal arbors.

Basic physiological characteristics were determined from voltage responses to square-wave current pulses of 500 ms duration, ranging from -100 pA to +400 pA, and delivered in 20 pA intervals. Input resistance was determined by the slope of the linear regression through the voltage-current curve. Sag was determined as the voltage difference between the lowest voltage response and the steady-state response at the last 50 ms to a square-wave current pulses of 500 ms duration at -100 pA. Single action potential (AP) characteristics were obtained from the first elicited action potential. AP threshold was defined as the inflection point at the foot of the regenerative upstroke. AP amplitude was defined as the voltage difference between the threshold and peak voltage. AP half-width was measured at half of the peak amplitude. AP rise time was quantified as duration from 10% to 90% of the peak amplitude. The fast after-hyperpolarizing potential (fAHP) amplitude was measured as the peak hyperpolarizing deflection from AP threshold following AP initiation. AP frequency was determined from the number of APs in response to a square-wave current pulse of 500 ms duration.

*Human.*

656 *Ex vivo* recordings of acutely resected frontal cortex were performed as  
657 previously described<sup>3</sup>. Non-eloquent overlaying tissue requiring surgical  
658 resection was utilized in order to access the location of a tumor. Immediately  
659 following resection, the tissue block was transferred to oxygenated (95% O<sub>2</sub>/5%  
660 CO<sub>2</sub>) ice-cold artificial cerebrospinal fluid (aCSF) containing (in mM) 127 NaCl,  
661 25 NaHCO<sub>3</sub>, 25 D-glucose, 2.5 KCl, 1.25 NaH<sub>2</sub>PO<sub>4</sub>, 1.5 MgSO<sub>4</sub> and 1.6 CaCl<sub>2</sub> during  
662 rapid transport to the laboratory. The time between surgical resection and tissue  
663 slicing was <10 min. Whole-cell recordings were performed similarly to mice as  
664 described above.

665

#### 666 *Fluorescence Immunohistochemistry*

##### 667 *Mouse.*

668 Deep anaesthesia was induced by intraperitoneal injection of  
669 pentobarbital, and mice were transcardially perfused with saline followed by 4%  
670 paraformaldehyde (PFA). Brains were dissected and post-fixed in 4% PFA for 2 h  
671 at room temperature. Brains were transferred into 10% sucrose phosphate  
672 buffer (PB 0.1 M, pH 7.3) and stored overnight at 4°C. Embedding was performed  
673 in a 12% gelatin/10% sucrose block, with fixation in 10%  
674 paraformaldehyde/30% sucrose solution (PB 0.1 M) for 2 h at room temperature  
675 and immersed in 30% sucrose (PB 0.1 M) at 4°C overnight. Forty micrometer  
676 coronal sections were collected serially (rostral to caudal) using a freezing  
677 microtome (Leica, Wetzlar, Germany; SM 2000R) and stored in 0.1 M PB.  
678 Sections were pre-incubated with a blocking PBS buffer containing 0.5% Triton  
679 X-100 and 10% normal horse serum (NHS; Invitrogen, Bleiswijk, The  
680 Netherlands) for 1 h at room temperature. Sections were incubated in a mixture

681 of primary antibodies in PBS buffer containing 0.4% Triton X-100 and 2% NHS  
 682 for 72 h at 4°C. The following primary antibodies were used:  
 683 mouse anti-PV (1:1000, Swant, 235, lot #10-11(F)); RRID:AB\_10000343  
 684 rabbit anti-PV (1:1000, Swant PV25); RRID:AB\_10000344  
 685 goat anti-MBP (1:300, Santa Cruz, C-16, sc-13914, lot #F2416);  
 686 RRID:AB\_648798  
 687 mouse anti-MBP (1:300, Santa Cruz, F-6, sc-271524); RRID:AB\_10655672  
 688 mouse anti-Ube3a (1:300, Sigma, 3E5, SAB1404508, lot #G4251-3E5);  
 689 RRID:AB\_10740376  
 690 rabbit anti-pS6<sup>S235/236</sup> (1:300, Cell Signaling Technologies, 2211S, lot  
 691 #23); RRID:AB\_331679  
 692 goat anti-SOM (1:300, Santa Cruz, D-20, sc-7819, lot #E1915);  
 693 RRID:AB\_2302603  
 694 mouse anti-APC [CC1] (1:200, Abcam, ab16794); RRID:AB\_443473  
 695 Sections were washed with PBS and incubated with corresponding Alexa-  
 696 conjugated secondary antibodies (1:300, Invitrogen) and cyanine dyes (1:300,  
 697 Sanbio, Uden, The Netherlands) in PBS buffer containing 0.4% Triton X-100, 2%  
 698 NHS for 2-5 h at room temperature. Sections were washed with PB 0.1 M and  
 699 mounted on slides, cover slipped with Vectashield H1000 fluorescent mounting  
 700 medium (Vector Labs, Peterborough, UK), sealed and imaged  
 701 Recovery of biocytin-labelled cells following electrophysiological  
 702 recordings was performed as reported before<sup>3</sup>, with minor alterations.  
 703 Specifically, 300 µm slices were incubated overnight at 4°C in fresh 4%  
 704 paraformaldehyde (PFA). Slices were extensively rinsed at room temperature in  
 705 PBS and stained in PBS buffer containing 0.4% Triton X-100, 2% normal horse

serum (NHS; Invitrogen, Bleiswijk, The Netherlands) and streptavidin-  
conjugated secondary antibody (1:300, Jackson; for PV::cre,Ai14-labelled and  
SOM::cre,Ai14-labelled cells) or streptavidin-Cy3 (1:300; Invitrogen; for GFP-  
labelled cells) overnight at 4°C. Slices were washed with PBS and PB 0.1 M and  
mounted on slides, cover slipped with 150 µl Mowiol (Sigma), sealed, and  
imaged for their axonal morphology (see **Confocal Microscopy and Analysis**).  
To avoid excessive thinning or dehydration of 300 µm sections, cells were  
mounted, immediately imaged and returned to PB 0.1 M directly after imaging.

After full cell imaging, 300 µm slices were extensively washed in PB 0.1 M  
and incubated overnight at 4°C in 30% sucrose (0.1 M PB). Sections were then  
carefully recut at 40 µm using a freezing microtome (Leica, Wetzlar, Germany;  
SM 2000R) and stored serially in 0.1 M PB at 4°C. Serial 40 µm sections were  
extensively washed with PBS and pre-incubated with a blocking PBS buffer  
containing 0.5% Triton X-100 and 10% NHS for 1 h at room temperature.  
Sections were incubated in PBS buffer containing 0.4% Triton X-100 and 2%  
NHS for 72 h at 4°C and goat anti-MBP. Then, sections were washed with PBS,  
and incubated with corresponding Alexa-conjugated secondary antibodies  
(1:300, Invitrogen) and cyanine dyes (1:300, Sanbio, Uden, The Netherlands) in  
PBS buffer containing 0.4% Triton X-100, 2% NHS for 5 h at room temperature.  
For biocytin, streptavidin-A488 (1:300, Jackson) and streptavidin-Cy3 (1:300,  
Invitrogen) were additionally used. Sections were washed with PB 0.1M and  
mounted on slides, cover slipped with Vectashield H1000 fluorescent mounting  
medium (Vector Labs, Peterborough, UK), sealed and imaged.

*Human Tissue.*

Three-hundred  $\mu\text{m}$  electrophysiology slices with biocytin-labelled cells were incubated overnight at  $4^{\circ}\text{C}$  in 4% PFA. Slices were stained with secondary streptavidin-Cy3 (1:300, Sanbio, Uden, The Netherlands) in PBS buffer containing 0.5% Triton X-100 and 1% BSA for 5 h at room temperature. Next, three-hundred thick images were taken with confocal microscopy (**see Confocal Imaging and Analysis**). Slices were then rinsed at room temperature in 0.1 M PB, incubated for 16 h at  $4^{\circ}\text{C}$  in 10% sucrose (0.1 M PB), and overnight at  $4^{\circ}\text{C}$  in 30% sucrose (0.1 M PB). Forty  $\mu\text{m}$  sections were collected serially using a freezing microtome (Leica, Wetzlar, Germany; SM 2000R) and stored in 0.1 M PB. Sections were extensively washed and pre-incubated with a blocking PBS buffer containing 0.5% Triton X-100 and 5% bovine serum albumin (BSA; Sigma-Aldrich, The Netherlands) for 1 h at room temperature. Next, sections were incubated in a mixture of primary antibodies in PBS buffer containing 0.5% Triton X-100 and 1% BSA for 72 h at  $4^{\circ}\text{C}$ . The following primary antibodies were used: mouse anti-MBP (1:300, Santa Cruz, F-6, sc-271524).

Sections were extensively washed with PBS ( $>2$  h), and incubated with corresponding Alexa-conjugated secondary antibodies (1:300, Invitrogen), and streptavidin-cyanine dyes (1:300, Sanbio, Uden, The Netherlands) in PBS buffer as previously described. Sections were washed with PB 0.1 M and mounted on slides, cover slipped with Vectashield H1000 fluorescent mounting medium (Vector Labs, Peterborough, UK) and sealed.

### *Confocal Imaging and Analysis*

Confocal imaging was performed using a Zeiss LSM 700 microscope (Carl Zeiss) equipped with Plan-Apochromat 10x/0.45 NA, 40x/1.3 NA (oil

immersion) and 63x/1.4 NA (oil immersion) objectives. Alexa405/DAPI, Alexa488, Cy3/mCherry/tdTomato, and Alexa647 were imaged using excitation wavelengths of 405, 488, 555, and 639, respectively.

Quantification of interneuron-specific deletion of *Tsc1* or *Ube3a* as well as cell size analyses were performed in the prelimbic region in both hemispheres of the mPFC (bregma: +2.10 till +1.54 mm). We obtained tiled z-stack images (2048 x 2048 pixels) at 40x magnification with 1x digital zoom at a step size of 1  $\mu$ m. Stacks were randomly sampled across layers II-V. For quantification of deletion efficiency, immunofluorescent somatic co-localization of PV or SOM and pS6<sup>S235/236</sup> or Ube3a was manually-counted using NIH ImageJ (version 1.41). At least three z-stacks were analyzed per mouse. For quantification of cell size, outlines of non-overlapping PV+ or SOM+ cell bodies were manually drawn and area and outline were calculated using Measure function of ImageJ. Cells were *post hoc* divided into pS6+ and pS6- or Ube3a+ and Ube3a- groups and compared.

Density of PV+, SOM+ and CC1+ cells were measured in the prelimbic area of the mPFC (bregma +2.20 till +1.70) in brain slices obtained from transcardially perfused animals. For PV+ cell counts, single plane 3x3 tile scan (1789 x 1789  $\mu$ m) confocal images were obtained using the 10x objective with 1x digital zoom. All images captured both hemispheres. A 750 x 800  $\mu$ m counting frame was established bilaterally from the midline. Within this counting frame, cells were manually counted utilizing the multi-point tool (Fiji image analysis software, version 2.0.0). Cell density was calculated in standardized 10<sup>4</sup>  $\mu$ m<sup>2</sup> fields of view. SOM+ and CC1+ cell counts were performed using single plane 6x3

tile scan (1767 x 896  $\mu\text{m}$ ) confocal images capturing both hemispheres, with a 20x objective and 1x digital zoom.

Overall myelination in the prelimbic area of the mPFC (bregma +2.20 to +1.70) was measured in brain slices obtained from transcardially perfused animals. To capture both hemispheres, single plain, 6x3 tile scans (1767 x 896  $\mu\text{m}$ ) were made using a 20x objective with 1x digital zoom. MBP+ fluorescent area was quantified by employing the particle analysis tool in Fiji image analysis software (version 2.0.0).

Axonal examinations of virally-labelled cells were obtained by 63x magnification with 1x digital zoom and a step size of 0.5  $\mu\text{m}$ . Cells were randomly sampled from layers II-V of the prelimbic area of the mPFC. Examination of occurrence of axonal myelination was performed offline using ImageJ. Axons were identified as the thinnest, smoothest, and most highly branched processes originating from either the soma or primary dendrite. In addition, axons seemed to branch at more obtuse  $\geq 90^\circ$  angles from one another, often turning back toward the soma, whereas dendrites branched at smaller angles ( $< 90^\circ$ ), continuing their trajectory away from the soma. Additionally, SOM+ interneuron dendrites ubiquitously showed spines, whereas axons did not.

Axonal reconstructions of biocytin-filled cells were obtained at 63x magnification with 1x digital zoom and a step size of 0.5  $\mu\text{m}$ . Images were transferred to NeuroLucida 360 software (v2.8; MBF Bioscience) and reconstructed using interactive tracing with the Directional Kernels method. Reconstructed soma, axon and myelin segments were analyzed with NeuroLucida Explorer (MBF Bioscience). All reconstructed PV+ cells had a classic basket cell morphology<sup>30</sup>, for which none had a chandelier cell morphology. SOM+ cells

predominantly exhibited a Martinotti morphology<sup>30</sup> with an axonal arbor directed toward layer II-III. All SOM+ interneurons contained dendritic spines, whereas none of the PV+ interneurons did, including in any of the mutant lines.

Images for exact locations of all biocytin-filled cells (**Fig. 1-Figure Supplement 3**) were obtained at 10x magnification with 1x digital zoom, and distance from the center of the soma till the midline was measured using ImageJ.

Axons were considered to be myelinated when they exhibited at least one MBP-positive myelinated internode. Axons were considered to be unmyelinated when we could not identify a single MBP-positive myelinated internode across the axon up to at least the 7<sup>th</sup> branch order in mice and 10<sup>th</sup> branch order in human cells. The distance to first myelin was defined as the distance along the axon from the soma, or in the case of dendrite-originating axons the distance from the originating dendrite, to the initial point of MBP immunofluorescence. Myelin segments that exited a slice were removed from subsequent analysis. Distance from internodes till consecutive branch points were quantified from the center of the branch point till the onset of MBP immunofluorescence. Internodes that were not followed by a branch point – followed by another internode or an axonal segment that exited the slice – were not taken along for analysis.

No spatial corrections were made for tissue shrinkage.

### *Structured Illumination Microscopy (SIM) and Analysis*

Imaging was performed using a Zeiss Elyra PS1 system. 3D-SIM data was acquired using a 63x/1.4 NA (oil immersion) objective. 488, 561 and 642 100 mW diode lasers were used to excite the fluorophores together with respectively a BP 495-575 + LP 750, BP 570-650 + LP 75 or LP 655 emission filter. For 3D-



830 SIM imaging, a grating was present in the light path, modulated in 5 phases and 5  
831 rotations, and multiple z-slices with an interval of 110 nm were recorded on an  
832 Andor iXon DU 885, 1002x1004 EMCCD camera. Raw images were reconstructed  
833 using Zen 2012 software (Zeiss), and analyzed with NIH ImageJ and Fiji image  
834 analysis software.

835       To avoid overexposure and induce background minimization, images  
836 were taken starting from the edge of the soma or dendrite following along the  
837 first axonal branch order onward. Each axonal segment was imaged individually  
838 from branch point till the next branch point, with the experimenter blinded to  
839 the myelination status of the segments. Axonal segments that exited the slice  
840 were removed from further analysis. Axonal segments that were predominantly  
841 oriented in the z-axis (maximum z-range: ~15-20  $\mu\text{m}$ ) were not taken along for  
842 further analysis.

843       For structured branch diameter analysis, images were loaded into Fiji and  
844 analyzed analogously to previously reported<sup>13</sup> using custom-written software.  
845 Briefly, an average-intensity projection was applied on individual axonal  
846 segments. A confocal whole-cell overview image and full reconstruction were  
847 used to track the centrifugal branch order of each traced segment. Segments  
848 were traced from the center of a branch point along the axon till the center of the  
849 next branch point using the Simple Neurite Tracer plugin for Fiji.<sup>64</sup> Traces always  
850 followed the centrifugal direction away from the soma. Next, along the trace,  
851 perpendicular lines of 50 pixels (equals 2  $\mu\text{m}$ ) were placed on every pixel (~40  
852 nm) along the trace. On these perpendicular lines, biotin fluorescence intensity  
853 values were determined and a Gaussian curve was fitted on the intensity profile.  
854 Only fits with  $r^2 > 0.9$  were included in further analysis, resulting in a loss of

approximately ~10% of axonal pixel measurements. Subthreshold fits ( $r^2 < 0.9$ ) occurred due to occasional high background fluorescence, other processes in close proximity (axons/dendrites), extensive axon curvature, or rare axonal filopodia. Next, from the Gaussian fit the full width at half maximum (FWHM) was calculated. Consecutive FWHM values were not averaged, and individual pixel FWHM values are provided. Diameter profiles of full axon segments (excluding branch points and *en passant* boutons) were generated and analyzed further. Axonal segments that exited the slice before reaching the next branch point would be excluded from further analysis. Where applicable, after complete analysis segments were divided into unmyelinated and myelinated segments.

For comparative axon diameter analysis of PV+ and SOM+ interneurons in PV::TSC1, PV::UBE3A, PV::WT, SOM::TSC1 and SOM::WT, GFP-transduced cells from layers II till V were imaged, and the axon diameter of individual cells was determined at the start of the AIS at ~3-5  $\mu\text{m}$  from the soma or from the originating dendrite using FWHM measurements in Fiji. Similar to the detailed axon segment reconstructions, only measurements with fits  $>0.9$  were included in the analysis.

#### *mGFP-APEX2 Labeling, Electron Microscopy and Image Analysis.*

Adult heterozygous *Pvalb::cre* mice were unilaterally injected (see **Viral Labeling**) with AAV2/CAG-Flex-mGFP-APEX2 in a 0.5  $\mu\text{l}$  bolus undiluted with a titre of  $2.93 \times 10^{12}$  in the adult mPFC using the following coordinates: mPFC: +1.75 from bregma,  $\pm 0.35$  lateral, -1.9 dorsoventral (mm, from brain surface). After 7-14 days, mice were anesthetized by intraperitoneal injection of pentobarbital and transcardially perfused with saline followed by ice-cold 4%

paraformaldehyde (PFA)/1% glutaraldehyde in 0.1M PB. Brains were carefully dissected and post-fixed in the same solution overnight at 4°C. The brains were washed extensively in cold 0.1 M PB, and 100 µm coronal slices from the frontal cortex (bregma: +2.10 till +1.54 mm) were cut on a vibrating slicer (Microm HM 650V, Thermo Scientific). Sections were serially stored in cold 0.1M PB and processed for 3-3'-diaminobenzidine (DAB) staining.

Sections were incubated in full concentration DAB (0.1 M PB, 0.66% DAB, 0.033% H<sub>2</sub>O<sub>2</sub>) for 6 h at room temperature in the dark. Sections were washed in cold PB and post-fixed in cold 2% glutaraldehyde in 0.1 M PB for 2 hours at 4°C. Regions of interest were manually cut out and processed for electron microscopy. Samples were post-fixed in 1% osmium tetroxide, dehydrated, and embedded in epoxy resin. Ultrathin sections (40-60 nm) were cut on a Leica Ultramicrotome Supercut UCT, contrasted with uranyl acetate and lead citrate and analyzed in a Phillips CM100 electron microscopy (Aachen, Germany) at 80 kV. Multiple non-overlapping regions were imaged at 14kx and analyzed off-line using Fiji image software.

### *Statistical Analysis*

Statistical analysis was performed using IBM SPSS (version 23). Data sets were analyzed using Shapiro-Wilk test for normality. No outlier data were identified or removed. Experiments were designed using sample sizes comparable to previously published studies<sup>3,4</sup>. Masking was used for group allocation, data collection, and data analysis whenever possible. Data sets with normal distributions were analyzed for significance using unpaired Student's two-tailed *t*-test or analysis of variance (ANOVA) measures followed by Tukey's

*post hoc* test. Data are expressed as mean  $\pm$  standard error. Data sets with non-normal distributions were analyzed using Mann-Whitney *U* test or Kruskal-Wallis test with Dunn's adjustment for multiple comparisons.

Receiver operating characteristic (ROC) curves were generated using a custom-written algorithm to implement univariate<sup>14</sup> and bivariate<sup>65</sup> methods. Univariate and bivariate thresholds were determined at the corresponding points of maximization of the Youden's *J* statistic<sup>15</sup>, represented as the sum of the sensitivity and specificity. Area under the curve (AUC) values were computed as the integral of the univariate or bivariate ROC curves.

Exact *P*-values values are provided in the text, except when  $P < 0.001$ . Significance threshold was set at  $P < 0.05$ .

**Acknowledgements:** We thank the patients for their participation in this study, and the Erasmus MC neurosurgical team for facilitating the contribution of the tissue samples. Funding for this project was provided by the European Commission [NEURON-JTC2018-024, ERA-PerMed2018-127, H2020-FETPROACT-824070], Netherlands Organisation for Health Research and Development (ZonMW) [013.18.002, 40-00812-98-15030, 456.008.003], Netherlands Organization for Scientific Research (NWO) [NOCI Zwaartekracht 024.003.001], and Erasmus MC Desiderius Award to S.A.K., Erasmus MC Fellowship to Z.G.

## Figure Legends

**Figure 1.** Super-resolution microscopy of fast-spiking, PV+ interneuron axons. (a) Experimental approach. Biocytin-filled fast-spiking PV+ interneurons from mPFC were analyzed using both confocal imaging and structured illumination microscopy (SIM) imaging. See also **Fig. 1-Figure Supplement 1-3.** (b) Maximum projection confocal image of a representative biocytin-filled PV+ cell from mPFC layer V (red). Scale bar, 50  $\mu$ m. (c) Current clamp recording of evoked action potentials. Scale bars are 20 mV, 100 pA and 100 ms from top to bottom (right). (d) Full reconstruction of a mPFC layer V PV+ interneuron. Soma and dendrites in black, axon in brown. (e) Representative SIM z-stack projections of PV+ interneuron axonal segments (top), along with their corresponding FWHM diameter profiles (bottom). White arrowheads indicate measurement boundaries. From left to right: First branch order axon initial segment; second branch order unmyelinated axonal segment; third branch order myelinated axonal segment; sixth branch order unmyelinated axonal segment featuring multiple *en-passant* boutons (indicated by asterisks). Scale bar, 10  $\mu$ m. (f) Distribution histogram of PV+ interneuron axon shaft diameters, fitted with a Gaussian curve.  $n = 140$  axonal segments/8 cells. (g) Average axon shaft diameter decreases steadily over centrifugal branch order.  $n = 140$  segments/8 cells.  $P < 0.001$ , one-way ANOVA. (h) Distribution of axonal *en passant* bouton diameters of PV+ interneuron axons, fitted with a Gaussian curve.  $n = 250$  boutons/8 cells. Abbreviations: FWHM, full-width half-maximum. I, input current. SIM, structured illumination microscopy. Vm, membrane voltage.

**Figure 1-Figure Supplement 1.** Experimental flowchart for axonal

reconstructions.

**Figure 1-Figure Supplement 2.** Axonal diameter analysis. Interbranch axonal

diameter was sampled at high spatial frequency from branch point to branch

point. This representative example based on **Fig. 1e**, depicts a 3<sup>rd</sup> order branch

segment. **(a)** Axonal diameter was measured using the average intensity

projection of a z-stack series of SIM images (red). A semi-automated, user-guided

line was traced from the center of each axonal branch point to the center of the

subsequent distal branch point (thin white line). Each segment was analyzed in

the direction centrifugally oriented from the soma along the axon, as indicated

by the white arrow. For every consecutive 40 nm of axon, a 50-pixel wide line

(~2.0  $\mu\text{m}$ ) was drawn orthogonally to the tangent line of axonal orientation

(white). Scale bar, 5  $\mu\text{m}$ . **(b)** Along the orthogonals, pixel fluorescence intensities

were extracted (black diamonds) and a Gaussian line was fitted (grey). Fits with

$r^2 < 0.9$  were excluded from further analysis. From the Gaussian fit at each

consecutive axonal position, the full-width at half-maximum (FWHM) was

calculated. In this representative example, the FWHM (axonal diameter) = 0.238

$\mu\text{m}$  and  $r^2 = 0.987$ . **(c)** Left axis: Axonal diameter measurements as a function of

centrifugal distance along the axonal segment shown in **(a)**. Right axis: Fit ( $r^2$ ) of

the Gaussian function along the axonal segment. Black arrows indicate the

location of the corresponding fit shown in **(b)**. **(d)** Distribution over branch

order of median Gaussian fit ( $r^2$ ) prior to exclusion of points with  $r^2 < 0.9$ .

Individual cells in grey, average in black. **(e)** Goodness of fit ( $r^2$ ) is similar

between myelinated and unmyelinated segments. Individual cells in grey,  
average in black. Abbreviations: FWHM, full-width at half-maximum.

**Figure 1-Figure Supplement 3.** Locations of biocytin-filled and reconstructed PV+ and SOM+ cells. **(a)** Maximum projection confocal image of a biocytin-filled mPFC SOM+ interneuron (red), with the distance to midline indicated. **(b-e)** Soma locations of *Pvalb::cre*, Ai14 cells **(b)**, PV::UBE3A, PV::WT, PV::TSC1 cells **(c)**, *Sst::cre*, Ai14 cells **(d)**, and SOM::WT, SOM::TSC1 cells **(e)**. Black bars indicate mean  $\pm$  s.e.m.

**Figure 2.** PV+ interneuron axon diameter co-varies with myelination. **(a)** Average SIM z-stack projection of a biocytin-filled PV+ interneuron axon (red) along with its myelination (MBP; green arrowhead), centered over a fourth branch order segment. Note that the relatively thinner axonal segment is unmyelinated (white arrowhead). Scale bar, 5  $\mu$ m. **(b)** Average SIM z-stack projection of a biocytin-filled PV+ interneuron axon (red) lacking myelination (MBP), centered over a seventh branch order segment. Note the frequent *en passant* boutons and thin axon shaft. **(c)** Neurolucida reconstruction of an mPFC fast-spiking PV+ interneuron axon. Axon in grey, myelinated segments in green. Note the proximal onset of myelin, consisting of short internodes interspersed by branch points. **(d)** Frequency histogram of nearest neighbor distance from internodes to branch points.  $n = 81$  segments/5 cells. **(e)** Average axon segment diameter versus branch order, exclusively for segments showing myelination.  $n = 39$  segments/8 cells.  $P < 0.001$ , one-way ANOVA. **(f)** The joint combination of axonal diameter and interbranch point distance is highly predictive of segmental

1000 myelination. Each circle represents an individual axonal segment. Myelinated  
 1001 segments (green) are consistently thicker and longer compared to unmyelinated  
 1002 segments (black), with critical thresholds (dotted lines) of 13.4  $\mu\text{m}$  and 334 nm  
 1003 for interbranch distance and diameter, respectively.  $n = 140$  segments/8 cells.  
 1004 **(g)** Receiver-operator characteristic (ROC) curves for interbranch distance  
 1005 (blue) and diameter (red) as univariate predictors, as well as the significantly  
 1006 improved joint bivariate prediction (green) of myelination status ( $P < 0.001$ ).  
 1007 Diagonal dotted line indicates the non-discrimination reference boundary.  
 1008 Abbreviations: ROC, receiver-operator characteristic.  
 1009  
 1010 **Figure 3.** APEX2 contrast-enhanced electron microscopy confirms that smaller-  
 1011 diameter axonal segments lack myelination. **(a)** Experimental flowchart.  
 1012 *Pvalb::cre* mice were given unilateral injections into mPFC with AAV2/CAG-flex-  
 1013 mGFP-APEX2, and sacrificed for confocal and electron microscopy after 7 to 14  
 1014 days. **(b)** Confocal image of unilateral PV-specific mGFP-APEX2 expression in  
 1015 mPFC (green). White square depicts the region of interest in the prelimbic area.  
 1016 **(c)** Representative confocal microscopy image of mGFP-APEX2 fluorescence  
 1017 (green) and its colocalization with PV immunofluorescence (red). **(d)**  
 1018 Quantification of colocalization between mGFP-APEX2+ cells and PV  
 1019 immunofluorescence.  $93.9 \pm 1.3\%$  of mGFP-APEX2+ cells expressed PV.  $n = 2$   
 1020 mice **(e-f)** Electron microscopy images (14kx) of PV::mGFP-APEX2+ myelinated  
 1021 **(e)** and unmyelinated **(f)** axons (arrows). Morphological enlargements featuring  
 1022 mitochondria (asterisks) were not included in the diameter analysis. **(g)** PV+  
 1023 interneuron axonal segments featuring myelination have a larger average  
 1024 diameter (green) than unmyelinated axons (black). Unmyelinated:  $0.269 \pm 0.019$



$\mu\text{m}$ ,  $n = 38$ ; myelinated:  $0.570 \pm 0.045 \mu\text{m}$ ,  $n = 15$ . \*\*\*  $P < 0.001$ . Unpaired two-tailed Student's  $t$ -test. Black bars represent mean  $\pm$  s.e.m.

**Figure 4.** PV::TSC1 and PV::UBE3A mice exhibit reciprocal alterations of PV+ cell morphology. **(a)** Overview of mouse breeding scheme. **(b)** Maximum projection confocal image of PV+ somata (red) in PV::UBE3A mice lacking UBE3A (green; top), and in PV::TSC1 mice showing high pS6 expression (green, bottom). Higher magnification images are provided in **Fig. 4-Figure Supplements 1-2**. Scale bar, 15  $\mu\text{m}$ . **(c)** Quantification of PV+ interneuron maximum projection soma area from mPFC layers II-V. PV::UBE3A:  $92.1 \pm 2.7 \mu\text{m}^2$ ;  $n = 58$  cells; PV::WT:  $104.6 \pm 2.5 \mu\text{m}^2$ ;  $n = 109$  cells PV::TSC1:  $160.2 \pm 3.8 \mu\text{m}^2$ ;  $n = 159$  cells;  $n = 3$  mice per group. **(d)** Experimental procedure. PV::UBE3A, PV::WT and PV::UBE3A were stereotactically injected with AAV9/CAG-Flex-eGFP in the mPFC and analyzed two weeks later with SIM imaging. **(e)** Representative projection of a SIM z-stack showing primary axon branches (red) originating from transfected GFP+ somata in PV::UBE3A and PV::TSC1 mice. White arrowhead indicates location of axon onset. Scale bar, 2  $\mu\text{m}$ . **(f)** PV+ interneuron axon caliber quantifications from mPFC layers II-V. PV::UBE3A:  $0.613 \pm 0.023 \mu\text{m}$ ;  $n = 36$  axons; PV::WT:  $0.665 \pm 0.019 \mu\text{m}$ ;  $n = 46$  axons; PV::TSC1: pS6+  $0.846 \pm 0.034 \mu\text{m}$ ;  $n = 30$  axons;  $n = 3$  mice per group. \*\*\*  $P < 0.001$ ; \*\*  $P < 0.01$ ; \*  $P < 0.05$ . One-way ANOVA followed by *post hoc* Tukey's test. Black bars represent mean  $\pm$  s.e.m.

**Figure 4-Figure Supplement 1.** PV::TSC1 mice exhibit PV-specific deletion of *Tsc1*. **(a)** *Pvalb*::cre mice were crossed with floxed *Tsc1*<sup>f/f</sup> to obtain heterozygous *Pvalb*::cre x homozygous *Tsc1*<sup>-/-</sup> mice. In the absence of *Tsc1*, mTOR signaling is

disinhibited leading to excessive S6K activity. **(b)** Low magnification confocal image from the mPFC showing PV (red) and pS6<sup>235/236</sup> (green) immunofluorescence in adult mPFC, confirming the PV-specific increased S6K activity. **(c)** Maximum projection confocal image showing increased expression of pS6<sup>235/236</sup> (green) in most (arrows) but not all (asterisk) PV+ cells (red). Uncropped image from **Fig. 4b**. **(d)** Corresponding deletion of *Tsc1* was observed in  $83.8 \pm 3.6\%$  of PV+ cells,  $n = 3$  mice. **(e)**. High magnification confocal image showing a rare instance of an oddly shaped enlarged pS6+ PV::TSC1 cell (red). **(f)** Biocytin-filled PV::TSC1 cells (red) show short, thin filopodia (white arrowheads) radiating from the enlarged soma. Black bars indicate mean  $\pm$  s.e.m.

**Figure 4-Figure Supplement 2.** PV::UBE3A mice exhibit PV+ cell-specific deletion of *Ube3a*. **(a)** PV-specific knockout of *Ube3a*. **(b)** Low magnification confocal microscopy image showing immunofluorescence of Ube3a (green) and PV (red) in adult mPFC. Note that the remaining non-PV neuronal cell types still retain intact Ube3a expression. Scale bar, 10  $\mu$ m. **(c)** High magnification confocal image confirming the absence of Ube3a (green) in most (arrows) but not all (asterisk) PV+ cells (red). Uncropped image corresponding to **Fig. 4b**. **(d)** *Ube3a* was deleted in  $73.6 \pm 2.8\%$  of PV+ cells,  $n = 3$  mice. Black bars indicate mean  $\pm$  s.e.m.

**Figure 4-Figure Supplement 3.** PV cell-specific mutations of *Ube3a* or *Tsc1* do not alter PV+ cell density in mPFC. **(a)** Confocal microscopy image showing immunofluorescence of PV (red) and DAPI (white) in adult mPFC for PV::UBE3A, PV::WT, and PV::TSC1. Scale bar, 100  $\mu$ m. **(b)** Quantification of PV+ cell density. *P*

= 0.780, Kruskal-Wallis test owing to non-normality. Black bars indicate mean  $\pm$  s.e.m.

**Figure 4-Figure Supplement 4.** Electrophysiological properties of PV::TSC1, PV::WT, and PV::UBE3A cells. **(a)** input resistance.  $P = 0.741$ . **(b)** resting membrane potential.  $P = 0.267$ . **(c)** Frequency-current plot, in response to square-wave current steps.  $P = 0.999$ . PV::WT,  $n = 14$  cells; PV::TSC1,  $n = 22$  cells; PV::UBE3A,  $n = 16$  cells. **(d-h)** Analysis of the first action potential. **(d)** AP threshold.  $P = 0.518$ . **(e)** AP amplitude.  $P = 0.410$ . **(f)** fast afterhyperpolarization (fAHP) amplitude.  $P = 0.160$ . **(g)** AP rise time.  $P = 0.309$ . **(h)** AP half-width.  $P = 0.368$ . **(i-m)** Analysis of the first action potential. **(i)** AP threshold.  $P = 0.696$ . **(j)** AP amplitude.  $P = 0.855$ . **(k)** fast afterhyperpolarization (fAHP) amplitude.  $P = 0.073$ . **(l)** AP rise time.  $P = 0.082$ . **(m)** AP half-width.  $P = 0.475$ . One-way ANOVA in **(a)**, **(b)**, **(d)**, **(e)**, **(g)**, **(h)**, **(i)**, **(j)**, **(l)**, and **(m)**. Mann-Whitney  $U$  test in **(f)** and **(k)**. Repeated measures ANOVA in **(c)**. Black bars indicate mean  $\pm$  s.e.m. Abbreviations: AP, action potential; fAHP, fast afterhyperpolarization.

**Figure 5.** PV::UBE3A and PV::TSC1 mice exhibit bi-directional alterations in PV+ interneuron axonal myelination. **(a)** Experimental approach. Biocytin-filled fast-spiking PV+ interneurons from each genotype were first analyzed using confocal imaging. **(b-d)** Maximum projection image of a representative biocytin-filled PV+ cell (red, top), a close-up of a biocytin-filled somata (red, bottom), with a corresponding fast-spiking action potential train for PV::UBE3A **(b)**, PV::WT **(c)**, and PV::TSC1 **(d)**. Scale bars are 50  $\mu\text{m}$  (left) and 20 mV, 100 pA and 100 ms from top to bottom (right). **(e)** Representative SIM z-stack projection of a

1100 biocytin-filled PV+ interneuron axon centered over a 4<sup>th</sup> order branch (red),  
 1101 demonstrating myelinated (MBP, green; green arrowhead) and unmyelinated  
 1102 segments (white arrowhead). Scale bar, 5  $\mu$ m. **(f-h)** Proximal axon  
 1103 reconstructions (grey) including myelinated segments (green) of representative  
 1104 cells from PV::UBE3A **(f)**, PV::WT **(g)**, and PV::TSC1 **(h)** mice. **(i)** Nearly all PV+  
 1105 cells exhibit axonal myelination, independent of genotype. **(j-l)** PV+ cell-specific  
 1106 genetic manipulations bi-directionally alter myelin content **(j)**, internode length  
 1107 **(k)** and number of internodes per cell **(l)**. **(m)** The distribution of interbranch  
 1108 distance remains similar across genotypes ( $P = 0.575$ , repeated measures  
 1109 ANOVA group x branch order interaction). **(n)** Distance from the soma to the  
 1110 onset of myelination was unaffected by PV+ cell-specific deletion of *Ube3a* or  
 1111 *Tsc1*.  $P = 0.589$ , one-way ANOVA. **(o)** Experimental approach. Biocytin-filled fast-  
 1112 spiking PV+ interneurons from PV::UBE3A and PV::TSC1 mice were analyzed  
 1113 using both confocal and SIM imaging. **(p)** The joint combination of axonal  
 1114 diameter and interbranch point distance is highly predictive of PV::UBE3A cell  
 1115 segmental myelination. Critical thresholds (dotted lines) for interbranch  
 1116 distance and axonal diameter were 14.1  $\mu$ m and 332 nm, respectively.  $n = 49$   
 1117 segments/3 cells. Myelinated segments, green circles. Unmyelinated segments,  
 1118 black circles. **(q)** Receiver-operator characteristic (ROC) curve for PV::UBE3A  
 1119 cells. ROC curves of segmental myelination, comparing univariate models of  
 1120 interbranch distance (blue) and axonal diameter (red), and their joint bivariate  
 1121 combination (green). Diagonal dotted line indicates the non-discrimination  
 1122 reference boundary. **(r)** The joint combination of axonal diameter and  
 1123 interbranch point distance is highly predictive of PV::TSC1 cell segmental  
 1124 myelination. Critical thresholds (dotted lines) for interbranch distance and

axonal diameter were 18.6  $\mu\text{m}$  and 378 nm, respectively.  $n = 58$  segments/3 cells. Myelinated segments, green circles. Unmyelinated segments, black circles. (s) ROC curves for PV::TSC1 cells. ROC curves of segmental myelination, comparing univariate models of interbranch distance (blue) and axonal diameter (red), and their joint bivariate combination (green). Diagonal dotted line indicates the non-discrimination reference boundary. \*\*\* $P < 0.001$ , \*\* $P < 0.01$ , \* $P < 0.05$ , n.s. non-significant. One-way ANOVA in (j), (k), (l) and (n). Repeated measures ANOVA in (m). Black bars represent mean  $\pm$  s.e.m. Abbreviations: I, input current. ROC, receiver-operator characteristic. Vm, membrane voltage.

**Figure 5-Figure Supplement 1.** Intact global myelination and mature oligodendrocyte density in mPFC of mice with PV cell-specific mutations of *Ube3a* or *Tsc1*. (a) Confocal microscopy image showing immunofluorescence of MBP (green) and DAPI (white) for PV::UBE3A, PV::WT, and PV::TSC1. Scale bar, 100  $\mu\text{m}$ . (b) Quantification of MBP+ area.  $P = 0.256$ , Kruskal-Wallis test owing to non-normality. (c) Confocal microscopy image showing immunofluorescence of CC1+ mature oligodendrocytes (cyan) and DAPI (white) in adult mPFC for PV::UBE3A, PV::WT, and PV::TSC1. Scale bar, 100  $\mu\text{m}$ . (d) CC1+ mature oligodendrocyte density.  $P = 0.950$ . One-way ANOVA. Black bars indicate mean  $\pm$  s.e.m.

**Figure 6.** mPFC SOM+ interneurons have subthreshold axonal morphology and are correspondingly unmyelinated. (a) Experimental approach. Biocytin-filled regular-spiking SOM+ interneurons from mPFC were analyzed using both confocal imaging and SIM imaging. See also **Fig. 1-Figure Supplements 1-3.** (b)

1150 Maximum projection confocal image of a representative biocytin-filled SOM+  
 1151 interneuron (red). Scale bar, 50  $\mu$ m. (c) SOM+ interneuron recording  
 1152 demonstrating a low threshold for AP initiation, spike frequency adaptation, and  
 1153 AP amplitude attenuation. Scale bars are 20 mV, 100 pA and 100 ms from top to  
 1154 bottom. (d) Neurolucida reconstruction of the SOM+ cell depicted in (b). Soma  
 1155 and dendrite in black, axon in brown. Note the tortuous axonal arbor and  
 1156 dendrites. (e) mPFC SOM+ interneurons are rarely myelinated. Representative  
 1157 confocal image of a SOM+ interneuron axon (red), centered over a 3<sup>rd</sup> branch  
 1158 order segment (white arrowhead) without myelination (MBP, green; green  
 1159 arrowhead). Scale bar, 10  $\mu$ m. (f) Frequency histogram of SOM+ interneuron  
 1160 axon shaft diameter, fitted with a Gaussian curve.  $n = 88$  axonal segments/6 cells.  
 1161 (g) Axon shaft diameter decreases monotonically with increasing centrifugal  
 1162 branch order.  $n = 88$  segments/6 cells.  $P < 0.001$ , one-way ANOVA. (h)  
 1163 Distribution of axonal segment diameter and interbranch distances for  
 1164 myelinated (green circles) and unmyelinated (black circles) segments.  $n = 88$   
 1165 segments/6 cells. Dotted lines indicate the bivariate thresholds derived from  
 1166 *PV::WT* interneurons. Abbreviations: I, input current. Vm, membrane voltage.  
 1167  
 1168 **Figure 7.** SOM::*TSC1*+ cells are frequently myelinated. (a) Overview of mouse  
 1169 breeding scheme. (b) SOM::*TSC1*+ cells have enlarged somata. Left:  
 1170 Representative confocal images of SOM+ cells (red) confirm the increased  
 1171 expression of pS6 (green) in SOM::*TSC1* cells. Higher magnification images in  
 1172 **Fig. 7-Figure Supplement 1.** Right: SOM+ interneuron maximum projection  
 1173 soma area from mPFC layers II-V. SOM::*WT*:  $101.8 \pm 1.9 \mu\text{m}^2$ ,  $n = 81$  cells;  
 1174 *SOM::*TSC1**:  $166.4 \pm 3.7 \mu\text{m}^2$ ,  $n = 103$  cells;  $n = 3$  mice per group. \*\*\*  $P < 0.001$ .

1175 Unpaired two-tailed Mann-Whitney *U*-test. **(c)** Representative SIM z-stack  
 1176 projection images of GFP-labelled SOM+ interneuron axons (red). SOM::WT  
 1177 (top), SOM::TSC1 (bottom). Scale bar, 3  $\mu\text{m}$ . **(d)**. SOM::TSC1 cells have an  
 1178 increased axonal diameter. SOM::WT:  $0.799 \pm 0.049 \mu\text{m}$ ,  $n = 18$  cells; SOM::TSC1:  
 1179  $1.407 \pm 0.076 \mu\text{m}$ ,  $n = 17$  cells;  $n = 3$  mice per group. \*\*\*  $P < 0.001$ . Unpaired two-  
 1180 tailed Mann-Whitney *U*-test. **(e)** Experimental approach. Biocytin-filled regular-  
 1181 spiking SOM+ interneurons from mPFC of SOM::WT and SOM::TSC1 mice were  
 1182 analyzed using confocal imaging **(f)** Representative confocal z-stack projection  
 1183 image of a biocytin-filled SOM::TSC1 interneuron axon (red) and myelination  
 1184 (MBP), centered over a 7<sup>th</sup> branch order segment. Unmyelinated branch point  
 1185 indicated by white arrowhead. Scale bar = 10  $\mu\text{m}$ . **(g)** Neurolucida reconstruction  
 1186 of an mPFC SOM::TSC1 cell. The axon (grey) shows multiple myelinated  
 1187 internodes (green) along the main branch. Note the frequent thin, tortuous, and  
 1188 unmyelinated axon collaterals. **(h)** In contrast to SOM::WT cells, all 11  
 1189 reconstructed SOM::TSC1 cells were myelinated. **(i-k)** SOM::TSC1 cells exhibit a  
 1190 robust **(i)** total myelin ( $208.30 \pm 33.14 \mu\text{m}$ ), **(j)** number of internodes ( $6.97 \pm$   
 1191  $0.90 \mu\text{m}$ ), and **(k)** internode length ( $28.33 \pm 1.31 \mu\text{m}$ ). \*\*\* $P < 0.001$ , Unpaired  
 1192 Student's two-tailed *t*-test. SOM::WT:  $n = 6$ ; SOM::TSC1:  $n = 11$ . **(l)** Myelin  
 1193 segments occur with similar frequency on main SOM::TSC1 axon branches and  
 1194 axon collaterals ( $P = 0.99$ , Fisher's Exact Test). **(m)** Frequency histogram of  
 1195 nearest neighbor distance from internodes to branch points.  $n = 38$  segments/4  
 1196 cells. **(n)** Distance from the soma or originating dendrite to the onset of  
 1197 myelination was measurable only for SOM::TSC1 cells due to the very infrequent  
 1198 myelination of SOM::WT cells. **(o)** Experimental approach. Biocytin-filled  
 1199 regular-spiking SOM+ interneurons from SOM::TSC1 mice were analyzed using

1200 confocal and SIM imaging. **(p)** The joint combination of axonal diameter and  
 1201 interbranch point distance is highly predictive of PV::TSC1 cell segmental  
 1202 myelination. Critical thresholds (dotted lines) for interbranch distance and  
 1203 axonal diameter were 11.8  $\mu\text{m}$  and 406 nm, respectively.  $n = 86$  segments/5  
 1204 cells. Myelinated segments, green circles. Unmyelinated segments, black circles.  
 1205 **(q)** ROC curves for SOM::TSC1 cells. ROC curves of segmental myelination,  
 1206 comparing univariate models of interbranch distance (blue) and axonal diameter  
 1207 (red), and their joint bivariate combination (green). Diagonal dotted line  
 1208 indicates the non-discrimination reference boundary. Unpaired Student's two-  
 1209 tailed  $t$ -test in **(i)**, **(j)** and **(k)**. Unpaired two-tailed Mann-Whitney  $U$ -test in **(b)**  
 1210 and **(d)** owing to non-normality. Black bars represent mean  $\pm$  s.e.m.

1211 Abbreviations: ROC, receiver-operator characteristic.

1212

1213 **Figure 7-Figure Supplement 1.** SOM::TSC1 mice exhibit SOM-specific deletions  
 1214 of *Tsc1*. **(a)** *Sst::cre* mice were crossed with floxed *Tsc1<sup>fl/fl</sup>* to obtain heterozygous  
 1215 *Sst::cre* x homozygous *Tsc1<sup>-/-</sup>* mice (SOM::TSC1). In the absence of *Tsc1*, mTOR  
 1216 signaling is disinhibited leading to excessive S6K activity. **(b)** Maximum  
 1217 projection confocal image showing increased expression of pS6<sup>235/236</sup> (green) in  
 1218 most SOM::TSC1 cells (red). Uncropped image from **Fig. 7b**. **(c)** Maximum  
 1219 projection confocal image showing low expression of pS6<sup>235/236</sup> (green) in a  
 1220 minority of SOM::WT cells (red). Uncropped image from **Fig. 7b**. **(d)**  
 1221 Corresponding deletion of *Tsc1* was observed in  $95.8 \pm 2.1\%$  of cells,  $n = 3$  mice.  
 1222 **(e)** High magnification SIM image of a biocytin-filled cell confirming the presence  
 1223 of dendritic spines on SOM+ interneurons. Scale bar, 10  $\mu\text{m}$ . **(f)**  $r^2$  for FWHM  
 1224 Gaussian fits of SOM+ cell reconstructions. Median Gaussian fits ( $r^2$ ) over branch



order, prior to exclusion of points with  $r^2 < 0.9$ . Individual cells in grey, average in black. Black bars denote means  $\pm$  s.e.m.

**Figure 7-Figure Supplement 2.** SOM::TSC1 mice have a normal SOM+ cell density in mPFC. **(a)** Confocal microscopy image showing immunofluorescence of SOM (red) and DAPI (white) in adult mPFC for SOM::WT, and SOM::TSC1. Scale bar, 100  $\mu$ m. **(b)** SOM+ cell density in mPFC of SOM::TSC1 and SOM::WT mice.  $P = 0.416$ , Unpaired two-tailed Student's  $t$ -test. Black bars indicate mean  $\pm$  s.e.m.

**Figure 7-Figure Supplement 3.** Electrophysiological properties of SOM::TSC1 and SOM::WT cells. **(a)** input resistance.  $P = 0.018$ . **(b)** sag potential.  $P = 0.023$ . **(c)** resting membrane potential.  $P = 0.993$ . **(d)** AP threshold.  $P = 0.605$ . **(e)** AP amplitude.  $P = 0.994$ . **(f)** fast afterhyperpolarization (fAHP) amplitude.  $P = 0.915$ . **(g)** AP rise time.  $P = 0.639$ . **(h)** AP half-width.  $P = 0.265$ . **(i)** Frequency-current plot, in response to square-wave current steps.  $P < 0.001$ . SOM::WT,  $n = 6$  cells; SOM::TSC1,  $n = 13$  cells.  $*P < 0.05$  Unpaired two-tailed Student's  $t$ -test in **(a)** through **(f)** and **(i)**. Mann-Whitney  $U$  test in **(h)**. Repeated measures ANOVA in **(i)**. Black bars denote means  $\pm$  s.e.m. Abbreviations: AP, action potential; fAHP, fast afterhyperpolarization.

**Figure 8.** Extensive axonal myelination of SOM::TSC1 cells. **(a)** Experimental flowchart. Adult SOM::WT and SOM::TSC1 mice were injected with low-titer AAV9 cre-dependent GFP reporter virus in mPFC, and sacrificed 14 days later for MBP immunofluorescence labeling and confocal microscopy. **(b)** Maximum projection confocal image of a GFP-labelled SOM::TSC1+ interneuron showing

circumferential MBP expression (green). Scale bar, 5  $\mu$ m. **(c)** A high proportion of virally-labelled SOM::TSC1 cells exhibited myelination (92.0%, 46 of 50 cells), in contrast to SOM::WT cells (15.4%, 4 of 26 cells) ( $P < 0.001$ , Fisher's Exact Test). **(d)** Representative low-magnification confocal image from mPFC showing the robust increase of myelination (MBP, green) in SOM::TSC1 compared to SOM::WT mice. DAPI in white. Scale bar, 100  $\mu$ m. **(e)** Quantification of MBP+ area in mPFC of SOM::TSC1 mice ( $18.0 \times 10^6 \pm 3.6 \times 10^6$  A.U.) compared to SOM::WT mice ( $57.1 \times 10^6 \pm 4.8 \times 10^6$  A.U.).  $P < 0.001$ , Unpaired Student's two-tailed  $t$ -test. **(f)** Confocal microscopy image showing immunofluorescence of CC1 (cyan) and DAPI (white) in adult mPFC of SOM::WT and SOM::TSC1 mice. Scale bar, 100  $\mu$ m. **(g)** CC1+ cell density in adult mPFC of SOM::TSC1 and SOM::WT mice.  $P < 0.001$ , Unpaired Student's two-tailed  $t$ -test. Black bars indicate mean  $\pm$  s.e.m.

**Figure 9.** Myelination thresholds extend to fast-spiking interneurons in human cortex. **(a)** Experimental approach. Biocytin-filled interneurons from human *ex vivo* resected cortical tissue were analyzed using confocal imaging. **(b)** Maximum projection confocal image of a representative biocytin-filled human fast-spiking interneuron (red). Scale bar, 50  $\mu$ m. **(c)** Current clamp recording of evoked action potentials of human fast-spiking interneuron. Scale bars are 20 mV, 100 pA and 100 ms from top to bottom (right). **(d)** Full reconstruction of a human fast-spiking interneuron. Soma and dendrites in black, axon in brown. **(e)** Representative SIM z-stack projection image of a PV+ cell (biocytin, red), centered over a myelinated (MBP; green) 1<sup>st</sup> order axonal segment. Note that the myelinated axonal segment (green arrowhead) has a larger diameter than the unmyelinated axon segment (white arrowhead). **(f)** Representative SIM z-stack

projection featuring an unmyelinated segment of axon (red) centered over the 3rd branch order. Scale bar 10  $\mu\text{m}$  for (e) and (f). **(g)** Neurolucida reconstruction of a human fast-spiking interneuron axon. Axon in grey, myelinated segments in green. Since axon originated from proximal dendrite, dendrite is also depicted in brown. Note the proximal onset of myelin, consisting of short internodes interspersed by branch points. **(h)** Frequency histogram of nearest neighbor distance from internodes to branch points.  $n = 55$  segments/3 cells. **(i)** Experimental approach. Biocytin-filled interneurons from human *ex vivo* resected cortical tissue were analyzed using SIM imaging. **(j)** The joint combination of axonal diameter and interbranch point distance is highly predictive of human fast-spiking interneuron segmental myelination. Critical thresholds (dotted lines) for interbranch distance and axonal diameter were 13.7  $\mu\text{m}$  and 328 nm, respectively.  $n = 96$  segments/4 cells. Myelinated segments, green circles. Unmyelinated segments, black circles. **(k)** ROC curves for human fast-spiking interneurons. ROC curves of segmental myelination, comparing univariate models of interbranch distance (blue) and axonal diameter (red), and their joint bivariate combination (green). Diagonal dotted line indicates the non-discrimination reference boundary. Abbreviations: ROC, receiver-operator characteristic. I, input current. Vm, membrane voltage

**Supplementary Table 1.** Electrophysiological properties of *Pvalb::cre,Ai14* PV+ cells.

**Supplementary Table 2.** Electrophysiological properties of *Sst::cre,Ai14* SOM+ cells.

1300

1301 **Supplementary Table 3.** Electrophysiological properties of human fast-spiking  
1302 interneurons.

1303

1304 **Video 1.** Adult PV::TSC1 mice are ataxic. Left: PV::WT littermate. Right: PV::TSC1  
1305 mouse showing ataxia.

1306

## References

1. Simons, M. & Nave, K.-A. Oligodendrocytes: Myelination and Axonal Support. *Cold Spring Harb. Perspect. Biol.* (2015).  
doi:10.1101/cshperspect.a020479
2. Micheva, K. D. *et al.* A large fraction of neocortical myelin ensheathes axons of local inhibitory neurons. *Elife* **5**, e15784 (2016).
3. Stedehouder, J. *et al.* Fast-spiking Parvalbumin Interneurons are Frequently Myelinated in the Cerebral Cortex of Mice and Humans. *Cereb. Cortex* **39**, 1–13 (2017).
4. Stedehouder, J., Brizee, D., Shpak, G. & Kushner, S. A. Activity-dependent myelination of parvalbumin interneurons mediated by axonal morphological plasticity. *J. Neurosci.* (2018).  
doi:10.1523/JNEUROSCI.0074-18.2018
5. Duncan D. The importance of diameter as a factor in myelination. *Science (80-. ).* **79**, 363 (1934).
6. Hildebrand, C., Remahl, S., Persson, H. & Bjartmar, C. Myelinated nerve fibres in the CNS. *Prog. Neurobiol.* **40**, 319–384 (1993).
7. Lee, S. *et al.* A culture system to study oligodendrocyte myelination processes using engineered nanofibers. *Nat. Methods* **9**, 917–922 (2012).
8. Bechler, M. E., Byrne, L. & ffrench-Constant, C. CNS Myelin Sheath Lengths Are an Intrinsic Property of Oligodendrocytes. *Curr. Biol.* **25**, 2411–2416 (2015).
9. Goebbels, S. *et al.* A neuronal PI(3,4,5)P3-dependent program of oligodendrocyte precursor recruitment and myelination. *Nat. Neurosci.* **20**, 10–15 (2017).

- 1332 10. Auer, F., Vagionitis, S. & Czopka, T. Evidence for Myelin Sheath Remodeling  
1333 in the CNS Revealed by In Vivo Imaging. *Curr. Biol.* **28**, 549-559.e3 (2018).
- 1334 11. Hippenmeyer, S. *et al.* A developmental switch in the response of DRG  
1335 neurons to ETS transcription factor signaling. *PLoS Biol.* **3**, e159 (2005).
- 1336 12. Madisen, L. *et al.* A toolbox of Cre-dependent optogenetic transgenic mice  
1337 for light-induced activation and silencing. *Nat. Neurosci.* **15**, 793–802  
1338 (2012).
- 1339 13. Chéreau, R., Saraceno, G. E., Angibaud, J., Cattaert, D. & Nägerl, U. V.  
1340 Superresolution imaging reveals activity-dependent plasticity of axon  
1341 morphology linked to changes in action potential conduction velocity.  
1342 *Proc. Natl. Acad. Sci.* **114**, 1401–1406 (2017).
- 1343 14. Hanley, A. J. & McNeil, J. B. The Meaning and Use of the Area under a  
1344 Receiver Operating Characteristic (ROC) Curve. *Radiology* **143**, 29–36  
1345 (1982).
- 1346 15. Jin, H. & Lu, Y. The ROC region of a regression tree. *Stat. Probab. Lett.* **79**,  
1347 936–942 (2009).
- 1348 16. Karube, F. Axon Branching and Synaptic Bouton Phenotypes in GABAergic  
1349 Nonpyramidal Cell Subtypes. *J. Neurosci.* **24**, 2853–2865 (2004).
- 1350 17. Nörenberg, A., Hu, H., Vida, I., Bartos, M. & Jonas, P. Distinct nonuniform  
1351 cable properties optimize rapid and efficient activation of fast-spiking  
1352 GABAergic interneurons. *Proc. Natl. Acad. Sci.* **107**, 894–899 (2010).
- 1353 18. Hu, H. & Jonas, P. A supercritical density of Na(+) channels ensures fast  
1354 signaling in GABAergic interneuron axons. *Nat. Neurosci.* **17**, 686–93  
1355 (2014).
- 1356 19. Fu, C. *et al.* GABAergic Interneuron Development and Function Is

- 1357           Modulated by the Tsc1 Gene. *Cereb. Cortex* **22**, 2111–2119 (2012).
- 1358   20.   Normand, E. A. *et al.* Temporal and Mosaic Tsc1 Deletion in the Developing  
1359           Thalamus Disrupts Thalamocortical Circuitry, Neural Function, and  
1360           Behavior. *Neuron* **78**, 895–909 (2013).
- 1361   21.   Meikle, L. *et al.* A Mouse Model of Tuberous Sclerosis: Neuronal Loss of  
1362           Tsc1 Causes Dysplastic and Ectopic Neurons, Reduced Myelination,  
1363           Seizure Activity, and Limited Survival. *J. Neurosci.* **27**, 5546–5558 (2007).
- 1364   22.   Carson, R. P., Van Nielen, D. L., Winzenburger, P. A. & Ess, K. C. Neuronal  
1365           and glia abnormalities in Tsc1-deficient forebrain and partial rescue by  
1366           rapamycin. *Neurobiol. Dis.* **45**, 369–380 (2012).
- 1367   23.   Markus, A., Zhong, J. & Snider, W. D. Raf and Akt mediate distinct aspects of  
1368           sensory axon growth. *Neuron* **35**, 65–76 (2002).
- 1369   24.   Sidorov, M. S. *et al.* Enhanced Operant Extinction and Prefrontal  
1370           Excitability in a Mouse Model of Angelman Syndrome. *J. Neurosci.* **38**,  
1371           2671–2682 (2018).
- 1372   25.   Wallace, M. L., Burette, A. C., Weinberg, R. J. & Philpot, B. D. Maternal Loss  
1373           of Ube3a Produces an Excitatory/Inhibitory Imbalance through Neuron  
1374           Type-Specific Synaptic Defects. *Neuron* **74**, 793–800 (2012).
- 1375   26.   Judson, M. C. *et al.* Decreased axon caliber underlies loss of fiber tract  
1376           integrity, disproportional reductions in white matter volume, and  
1377           microcephaly in Angelman syndrome model mice. *J. Neurosci.* **37**, 7347–  
1378           7361 (2017).
- 1379   27.   Urban-Ciecko, J. & Barth, A. L. Somatostatin-expressing neurons in cortical  
1380           networks. *Nat. Rev. Neurosci.* **17**, 401–9 (2016).
- 1381   28.   Taniguchi, H. *et al.* A resource of Cre driver lines for genetic targeting of

1382 GABAergic neurons in cerebral cortex. *Neuron* **71**, 995–1013 (2011).

1383 29. Redmond, S. A. *et al.* Somatodendritic Expression of JAM2 Inhibits  
1384 Oligodendrocyte Myelination. *Neuron* **91**, 824–836 (2016).

1385 30. Jiang, X. *et al.* Principles of connectivity among morphologically defined  
1386 cell types in adult neocortex. *Science (80-. ).* **350**, aac9462 (2015).

1387 31. Stedehouder, J. & Kushner, S. A. Myelination of parvalbumin interneurons:  
1388 a parsimonious locus of pathophysiological convergence in schizophrenia.  
1389 *Mol. Psychiatry* **22**, 4–12 (2017).

1390 32. Tomassy, G. S. *et al.* Distinct profiles of myelin distribution along single  
1391 axons of pyramidal neurons in the neocortex. *Science* **344**, 319–24 (2014).

1392 33. Chong, S. Y. C. *et al.* Neurite outgrowth inhibitor Nogo-A establishes spatial  
1393 segregation and extent of oligodendrocyte myelination. *Proc. Natl. Acad.*  
1394 *Sci. U. S. A.* **109**, 1299–304 (2012).

1395 34. Freeman, S. A. *et al.* Acceleration of conduction velocity linked to clustering  
1396 of nodal components precedes myelination. *Proc. Natl. Acad. Sci. U. S. A.*  
1397 **112**, E321-8 (2015).

1398 35. Kann, O., Papageorgiou, I. E. & Draguhn, A. Highly energized inhibitory  
1399 interneurons are a central element for information processing in cortical  
1400 networks. *J. Cereb. Blood Flow Metab.* **34**, 1270–82 (2014).

1401 36. Lee, Y. *et al.* Oligodendroglia metabolically support axons and contribute  
1402 to neurodegeneration. *Nature* **487**, 443–8 (2012).

1403 37. Fünfschilling, U. *et al.* Glycolytic oligodendrocytes maintain myelin and  
1404 long-term axonal integrity. *Nature* **485**, 517–21 (2012).

1405 38. Saab, A. S. *et al.* Oligodendroglial NMDA Receptors Regulate Glucose  
1406 Import and Axonal Energy Metabolism. *Neuron* **91**, 119–32 (2016).



- 1407 39. Hu, H., Gan, J. & Jonas, P. Interneurons. Fast-spiking, parvalbumin<sup>+</sup>  
1408 GABAergic interneurons: from cellular design to microcircuit function.  
1409 *Science* **345**, 1255263 (2014).
- 1410 40. Strüber, M., Jonas, P. & Bartos, M. Strength and duration of perisomatic  
1411 GABAergic inhibition depend on distance between synaptically connected  
1412 cells. *Proc. Natl. Acad. Sci.* **112**, 201412996 (2015).
- 1413 41. Markram, H. *et al.* Interneurons of the neocortical inhibitory system. *Nat.*  
1414 *Rev. Neurosci.* **5**, 793–807 (2004).
- 1415 42. Timmler, S. & Simons, M. Grey matter myelination. *Glia* 1–8 (2019).  
1416 doi:10.1002/glia.23614
- 1417 43. Micheva, K. D. *et al.* Distinctive Structural and Molecular Features of  
1418 Myelinated Inhibitory Axons in Human Neocortex. *eNeuro* **5**, 1–12 (2018).
- 1419 44. Schmidt, H. *et al.* Axonal synapse sorting in medial entorhinal cortex. *Nat.*  
1420 *Publ. Gr.* **549**, 469–475 (2017).
- 1421 45. Tomassy, G. S. *et al.* Distinct Profiles of Myelin Distribution Along Single  
1422 Axons of Pyramidal Neurons in the Neocortex. *Science (80-. )*. **344**, 319–  
1423 324 (2014).
- 1424 46. Lundgaard, I. *et al.* Neuregulin and BDNF induce a switch to NMDA  
1425 receptor-dependent myelination by oligodendrocytes. *PLoS Biol.* **11**,  
1426 e1001743 (2013).
- 1427 47. Gautier, H. O. B. *et al.* Neuronal activity regulates remyelination via  
1428 glutamate signalling to oligodendrocyte progenitors. *Nat. Commun.* **6**,  
1429 (2015).
- 1430 48. Habermacher, C., Angulo, M. C. & Benamer, N. Glutamate versus GABA in  
1431 neuron–oligodendroglia communication. *Glia* 1–15 (2019).

doi:10.1002/glia.23618

49. Kougioumtzidou, E. *et al.* Signalling through AMPA receptors on oligodendrocyte precursors promotes myelination by enhancing oligodendrocyte survival. *Elife* **6**, 1–31 (2017).

50. Chen, T. J. *et al.* In Vivo Regulation of Oligodendrocyte Precursor Cell Proliferation and Differentiation by the AMPA-Receptor Subunit GluA2. *Cell Rep.* **25**, 852–861.e7 (2018).

51. Berret, E. *et al.* Oligodendroglial excitability mediated by glutamatergic inputs and Nav1.2 activation. *Nat. Commun.* **8**, (2017).

52. Makinodan, M., Rosen, K. M., Ito, S. & Corfas, G. A critical period for social experience-dependent oligodendrocyte maturation and myelination. *Science* **337**, 1357–60 (2012).

53. Zonouzi, M. *et al.* Individual Oligodendrocytes Show Bias for Inhibitory Axons in the Neocortex. *Cell Rep.* **27**, 2799–2808.e3 (2019).

54. Fields, R. D. A new mechanism of nervous system plasticity: activity-dependent myelination. *Nat. Rev. Neurosci.* **16**, 756–67 (2015).

55. Gibson, E. M. *et al.* Neuronal Activity Promotes Oligodendrogenesis and Adaptive Myelination in the Mammalian Brain. *Science (80-. ).* 1–16 (2014).

56. Mitew, S. *et al.* Pharmacogenetic stimulation of neuronal activity increases myelination in an axon-specific manner. *Nat. Commun.* **9**, 1–16 (2018).

57. Caputi, A., Melzer, S., Michael, M. & Monyer, H. The long and short of GABAergic neurons. *Curr. Opin. Neurobiol.* **23**, 179–186 (2013).

58. Melzer, S. *et al.* Distinct Corticostriatal GABAergic Neurons Modulate Striatal Output Neurons and Motor Activity. *Cell Rep.* **19**, 1045–1055 (2017).

- 1457 59. Rock, C., Zurita, H., Wilson, C. & Apicella, A. J. An inhibitory corticostriatal  
1458 pathway. *Elife* **5**, 1–17 (2016).
- 1459 60. Lee, A. T., Vogt, D., Rubenstein, J. L. & Sohal, V. S. A Class of GABAergic  
1460 Neurons in the Prefrontal Cortex Sends Long-Range Projections to the  
1461 Nucleus Accumbens and Elicits Acute Avoidance Behavior. *J. Neurosci.* **34**,  
1462 11519–11525 (2014).
- 1463 61. Dimou, L. & Simons, M. Diversity of oligodendrocytes and their  
1464 progenitors. *Curr. Opin. Neurobiol.* **47**, 73–79 (2017).
- 1465 62. Spitzer, S. O. *et al.* Oligodendrocyte Progenitor Cells Become Regionally  
1466 Diverse and Heterogeneous with Age. *Neuron* **101**, 459–471.e5 (2019).
- 1467 63. Judson, M. C. *et al.* GABAergic Neuron-Specific Loss of Ube3a Causes  
1468 Angelman Syndrome-Like EEG Abnormalities and Enhances Seizure  
1469 Susceptibility. *Neuron* **90**, 56–69 (2016).
- 1470 64. Longair, M. H., Baker, D. A. & Armstrong, J. D. Simple Neurite Tracer : open  
1471 source software for reconstruction , visualization and analysis of neuronal  
1472 processes. **27**, 2453–2454 (2018).
- 1473 65. Wang, M. C. & Li, S. ROC analysis for multiple markers with tree-based  
1474 classification. *Lect. Notes Stat.* **215**, 179–198 (2015).
- 1475

Figure 1

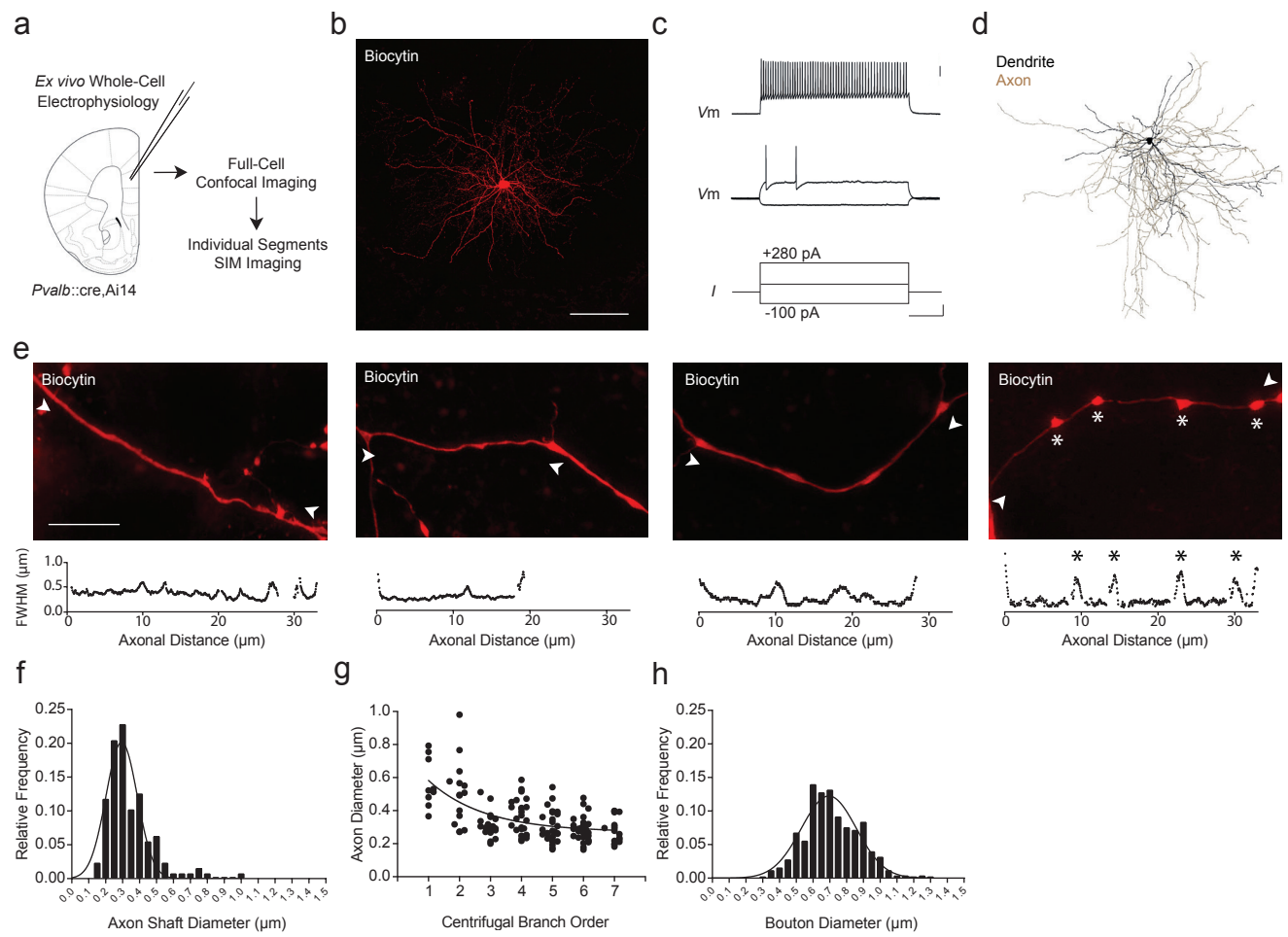


Figure 1 - Figure Supplement 1

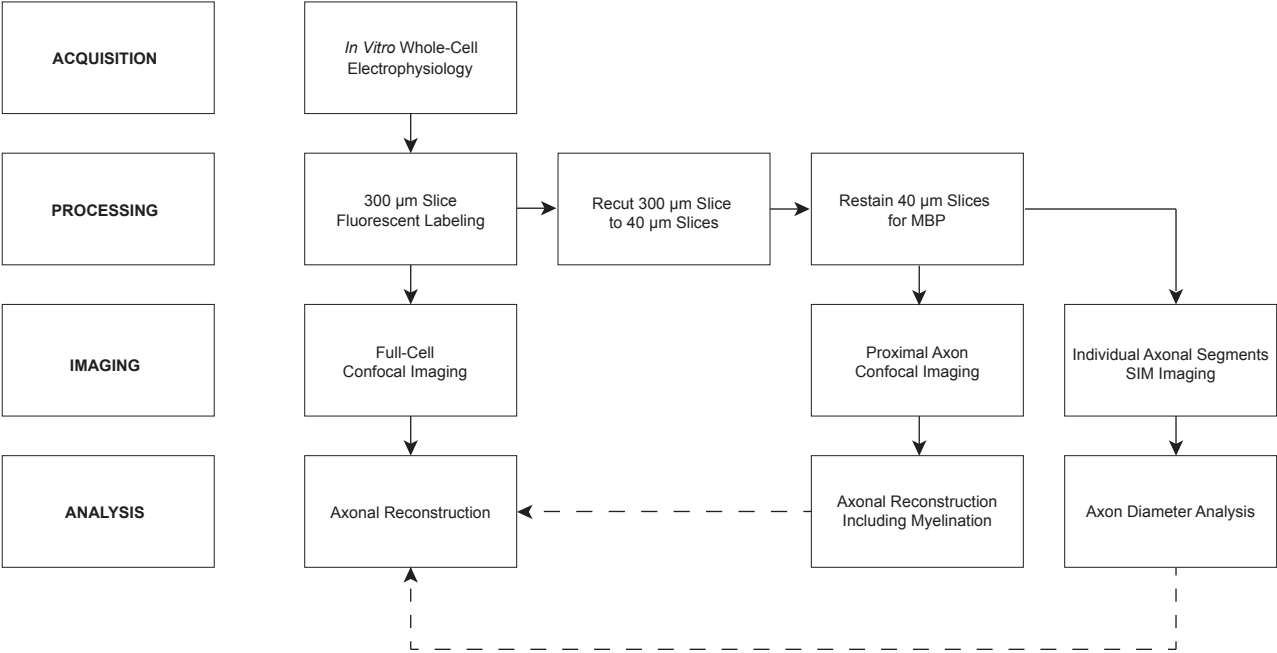


Figure 1 - Figure Supplement 2

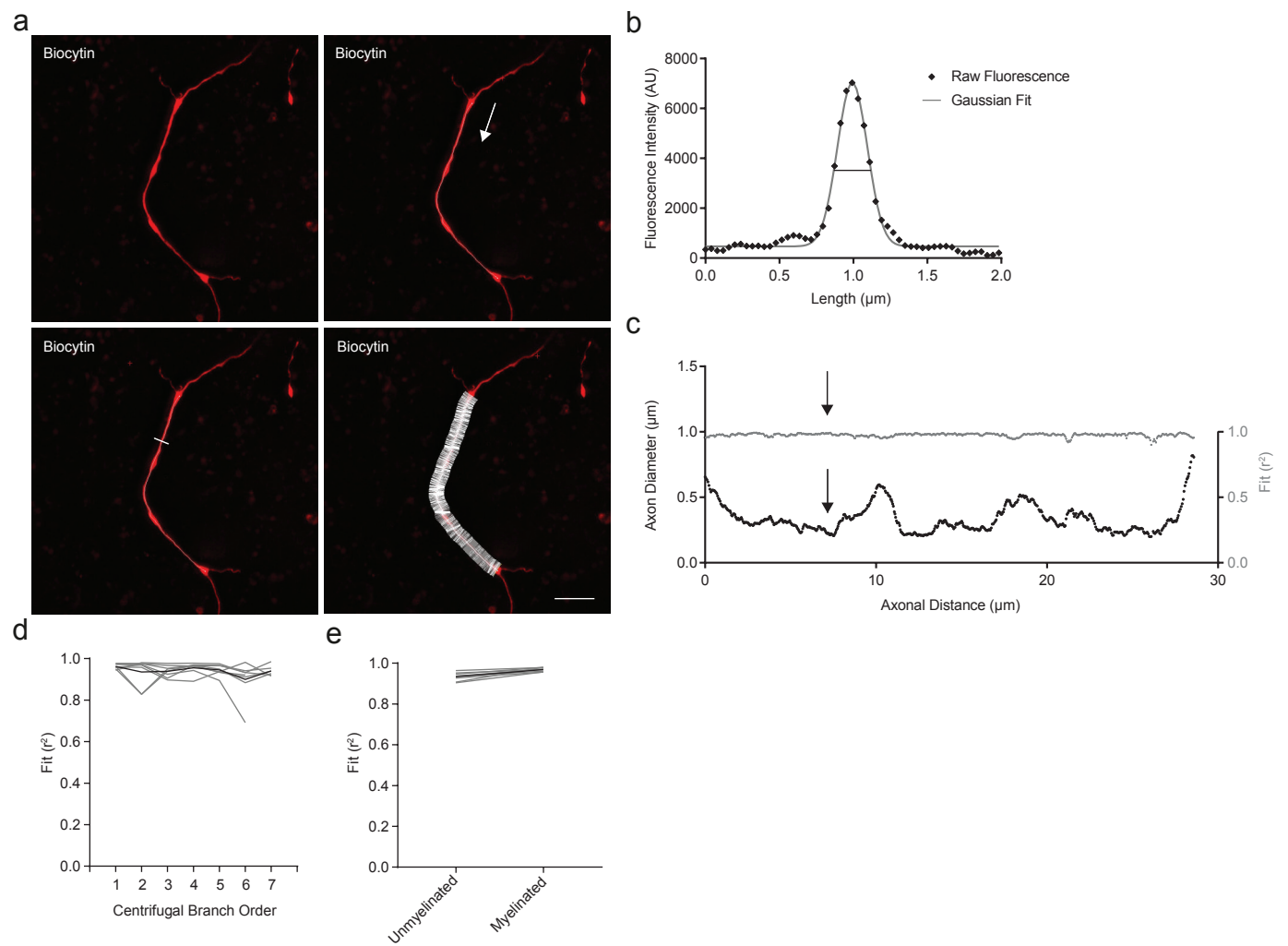


Figure 1 - Figure Supplement 3

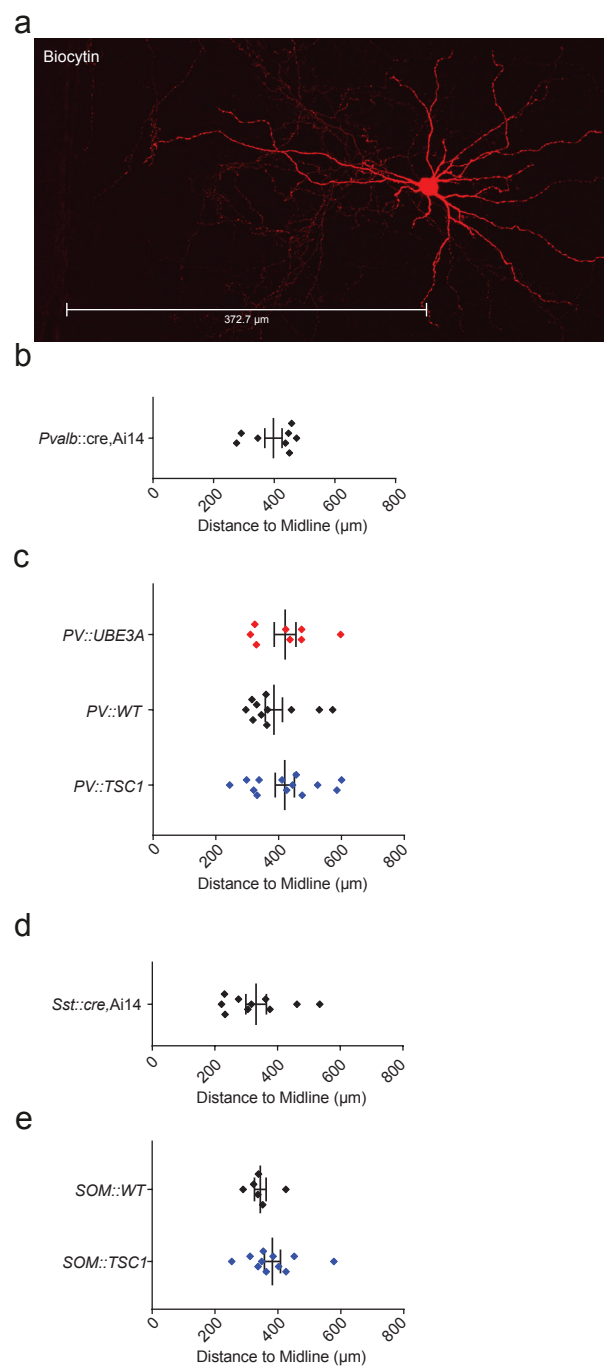


Figure 2

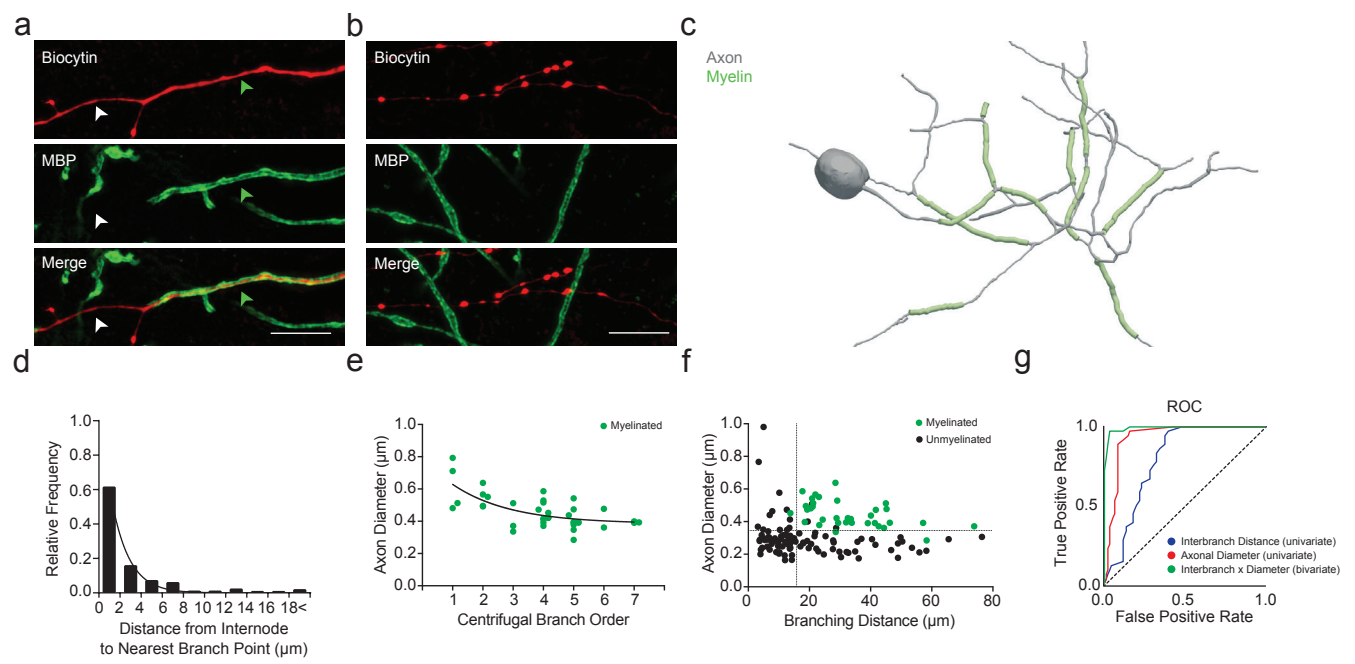




Figure 3

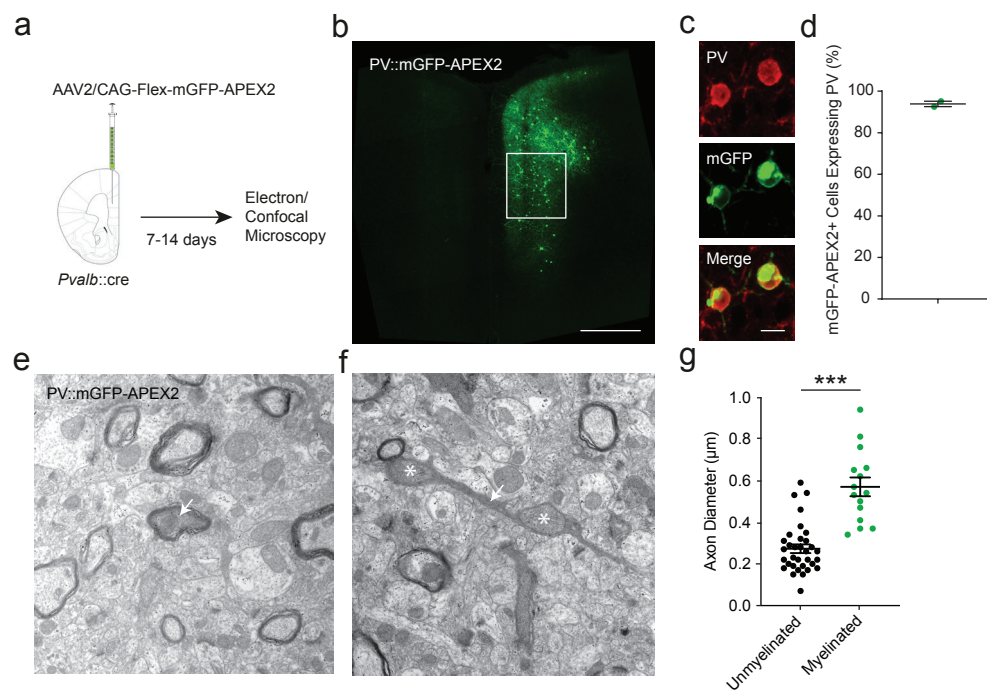


Figure 4

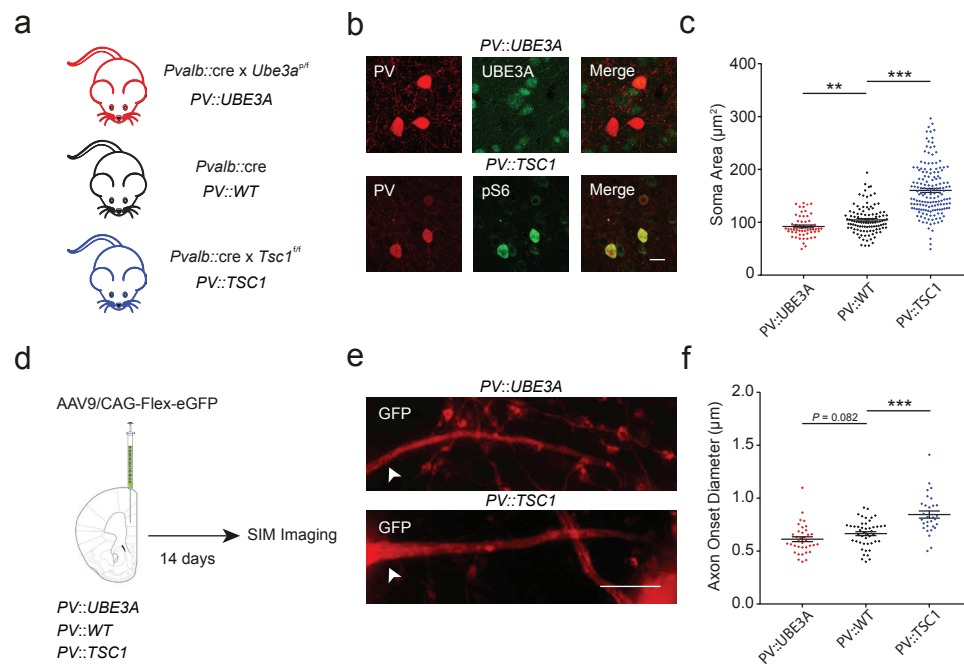


Figure 4 - Figure Supplement 1

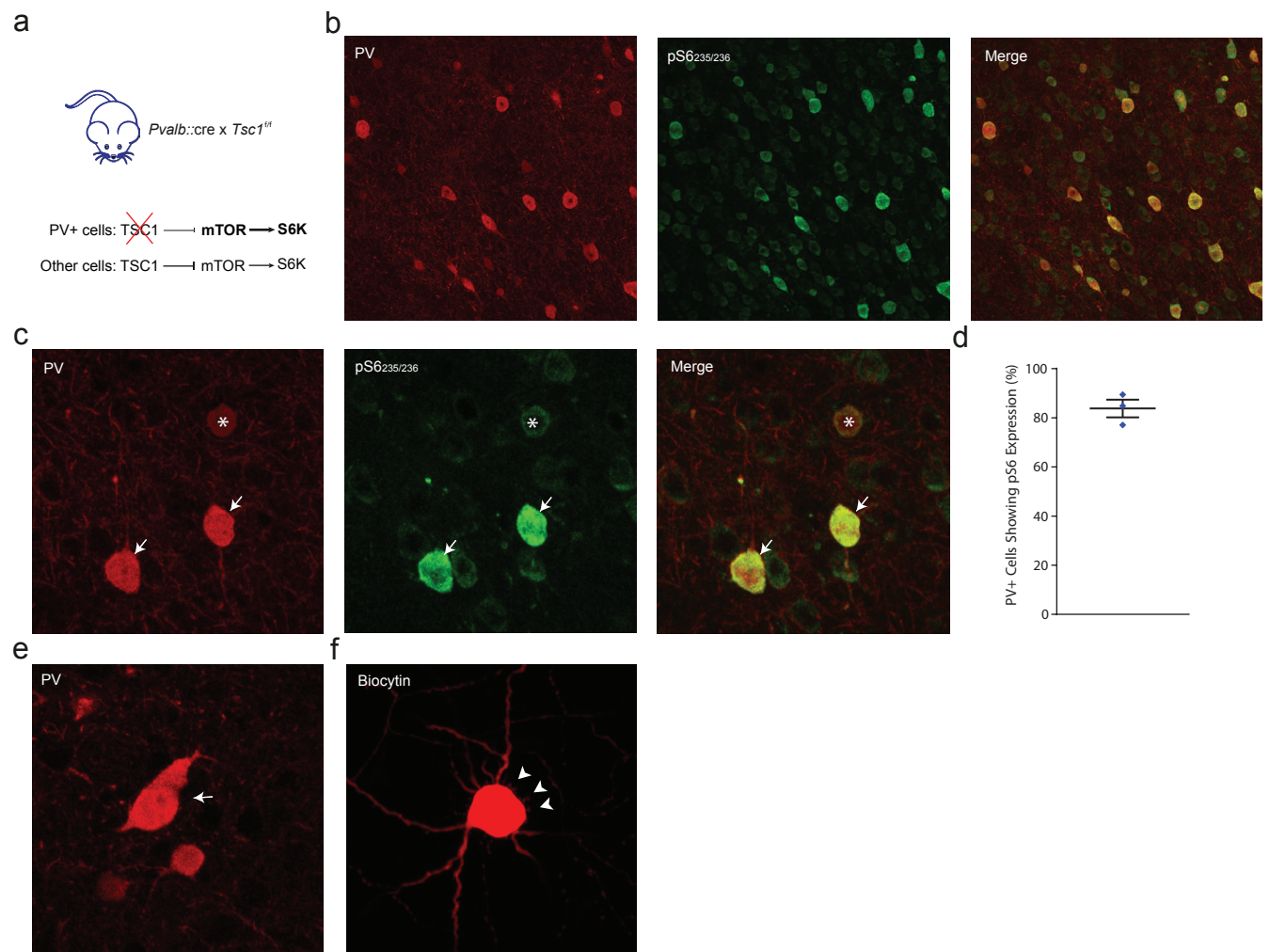


Figure 4 - Figure Supplement 2

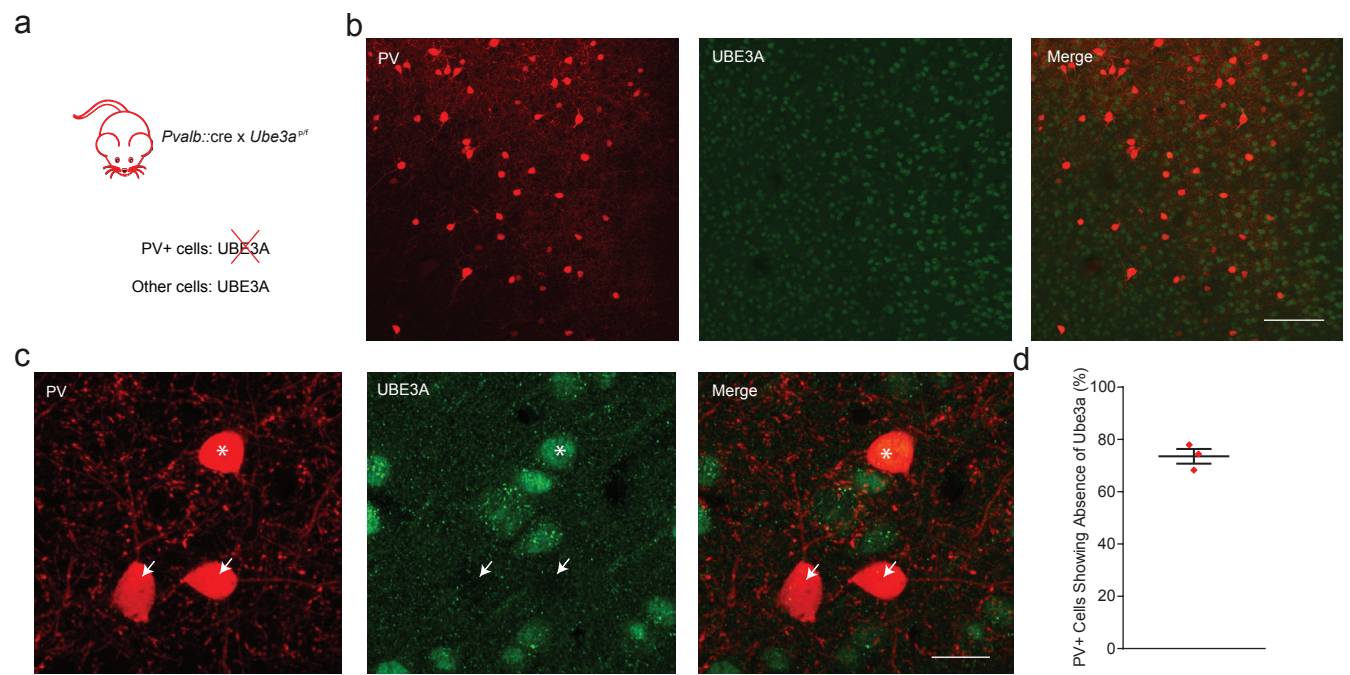


Figure 4 - Figure Supplement 3

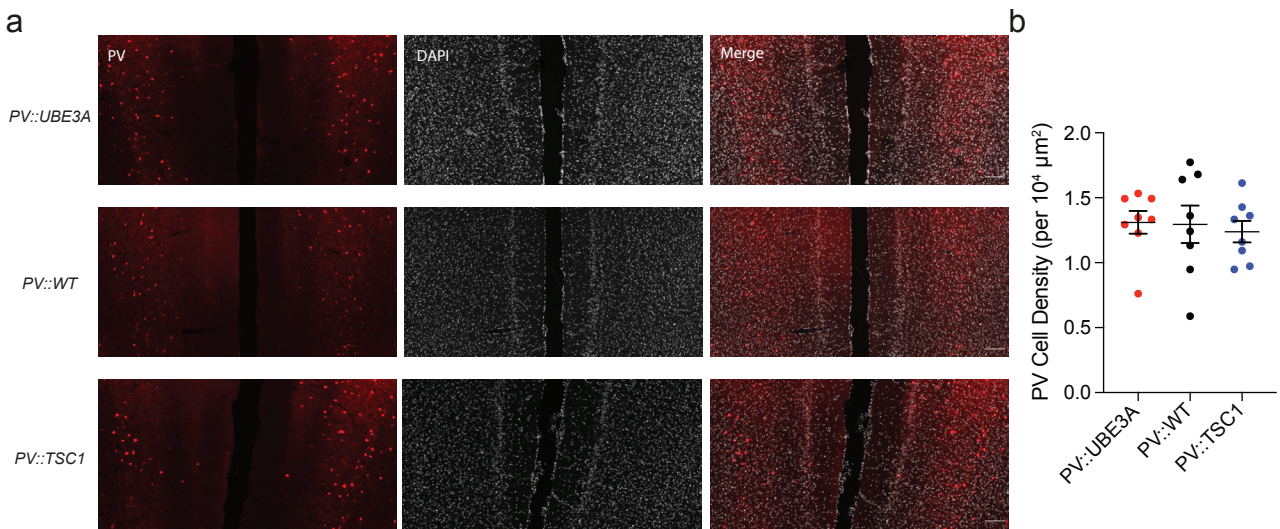


Figure 4 - Figure Supplement 4

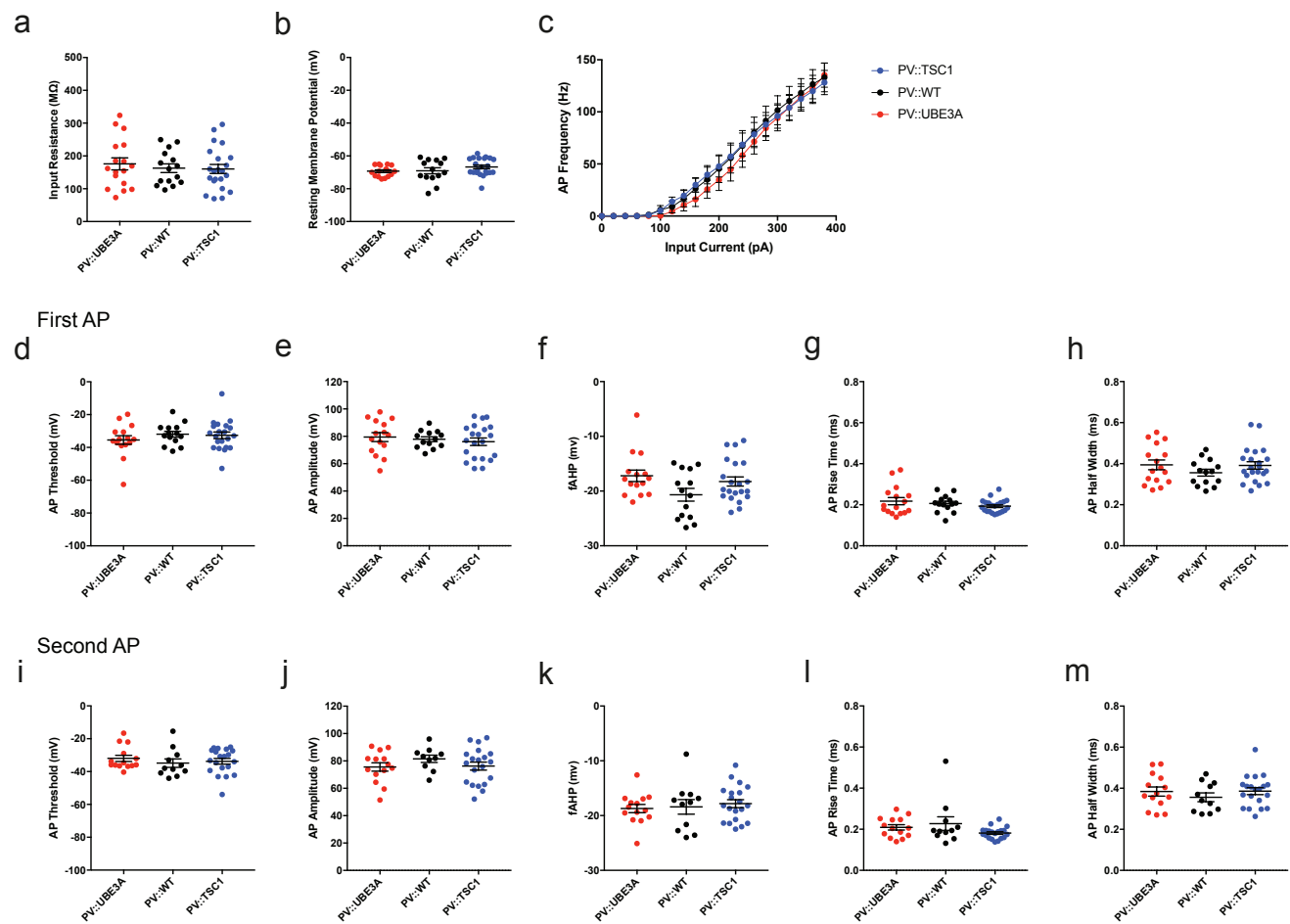




Figure 5

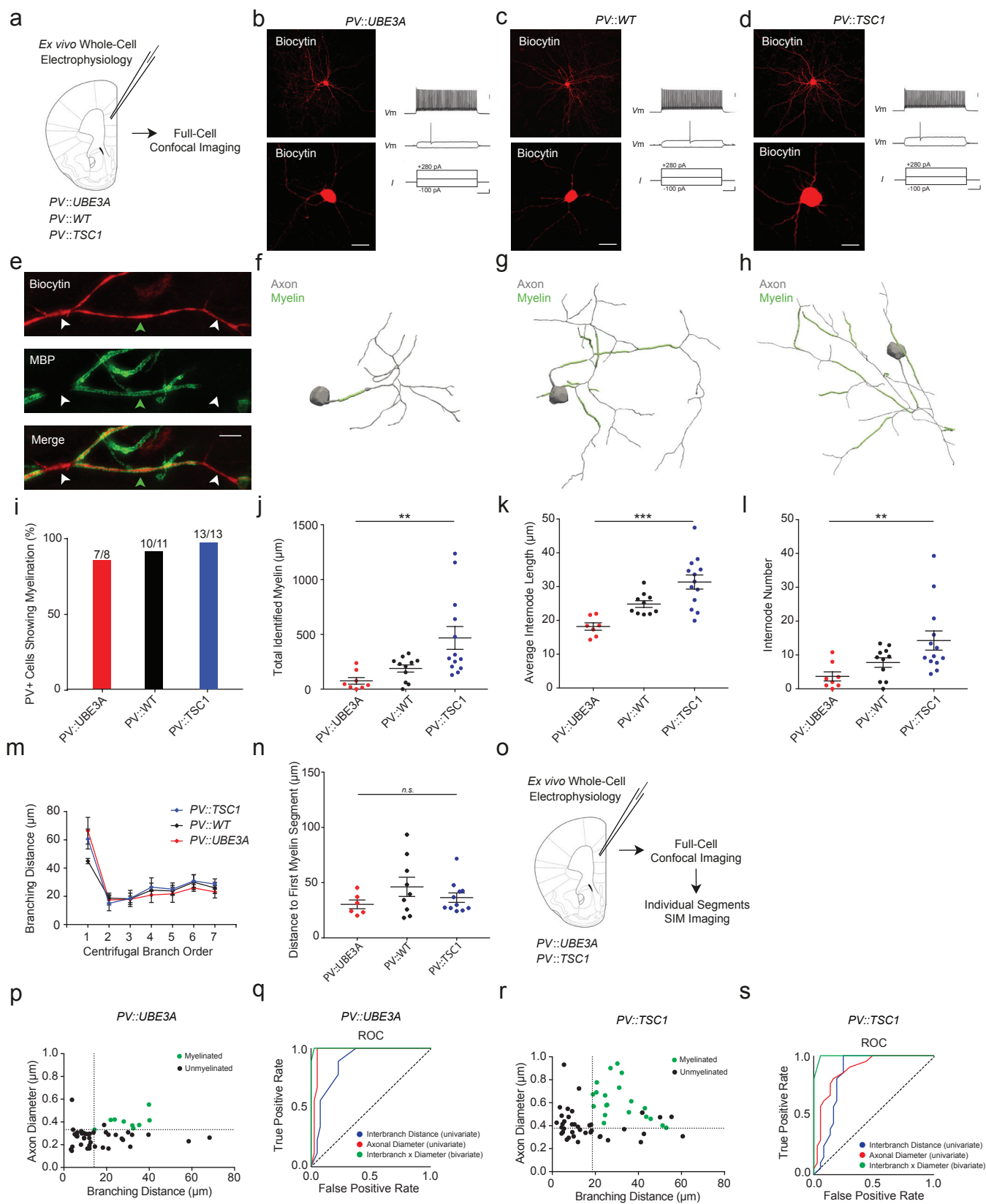


Figure 5 - Figure Supplement 1

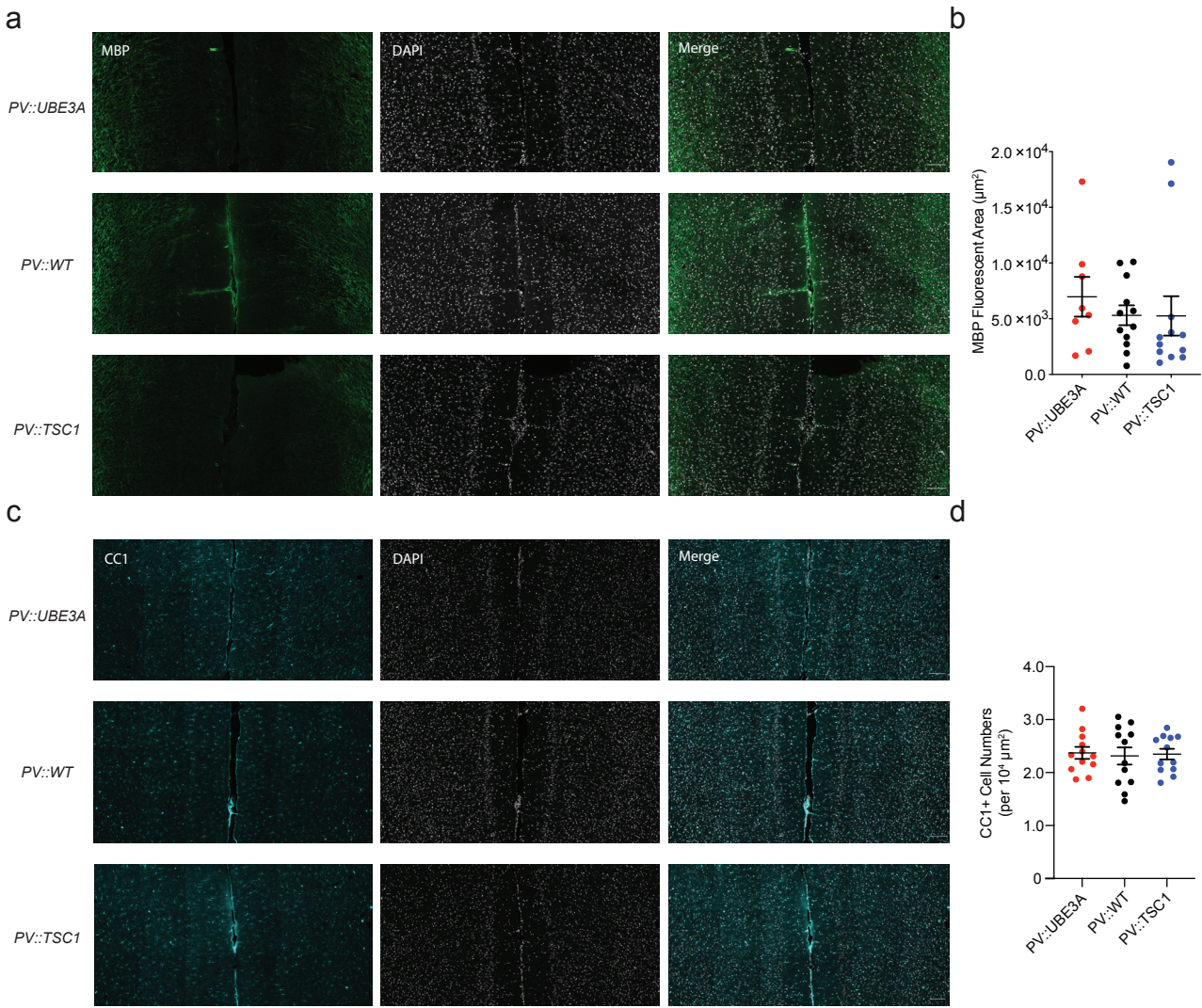




Figure 6

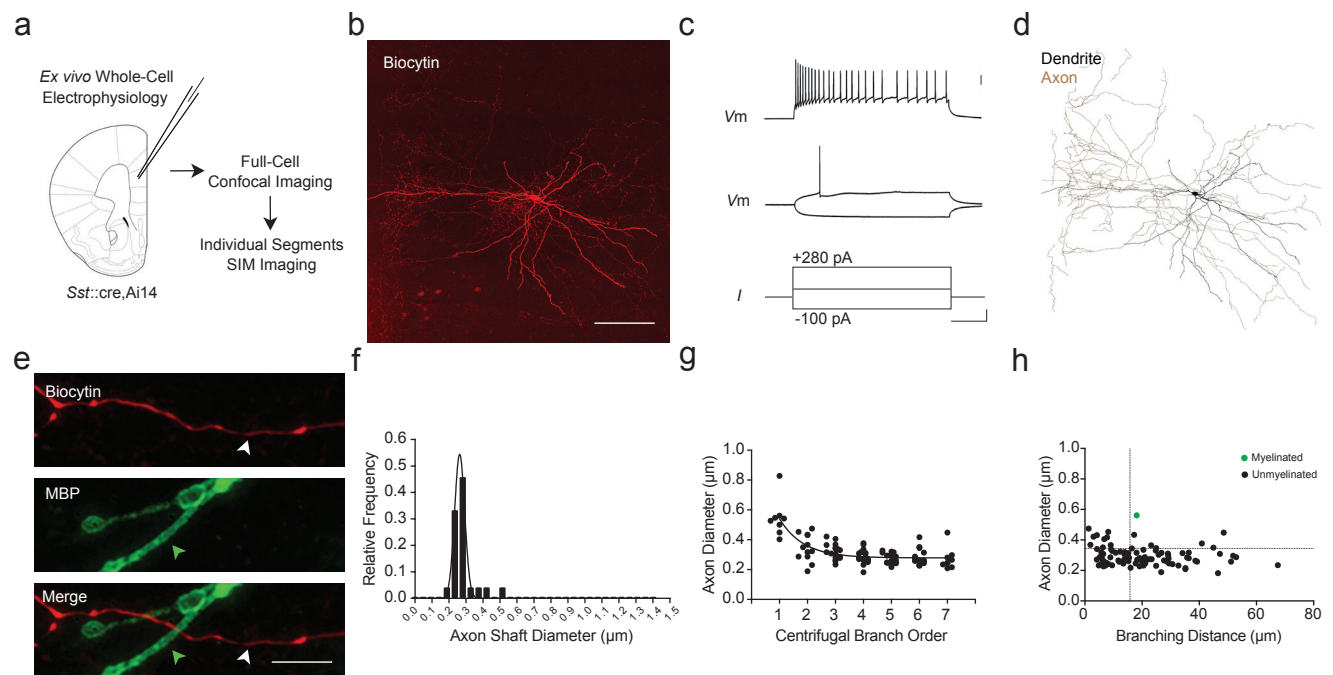


Figure 7

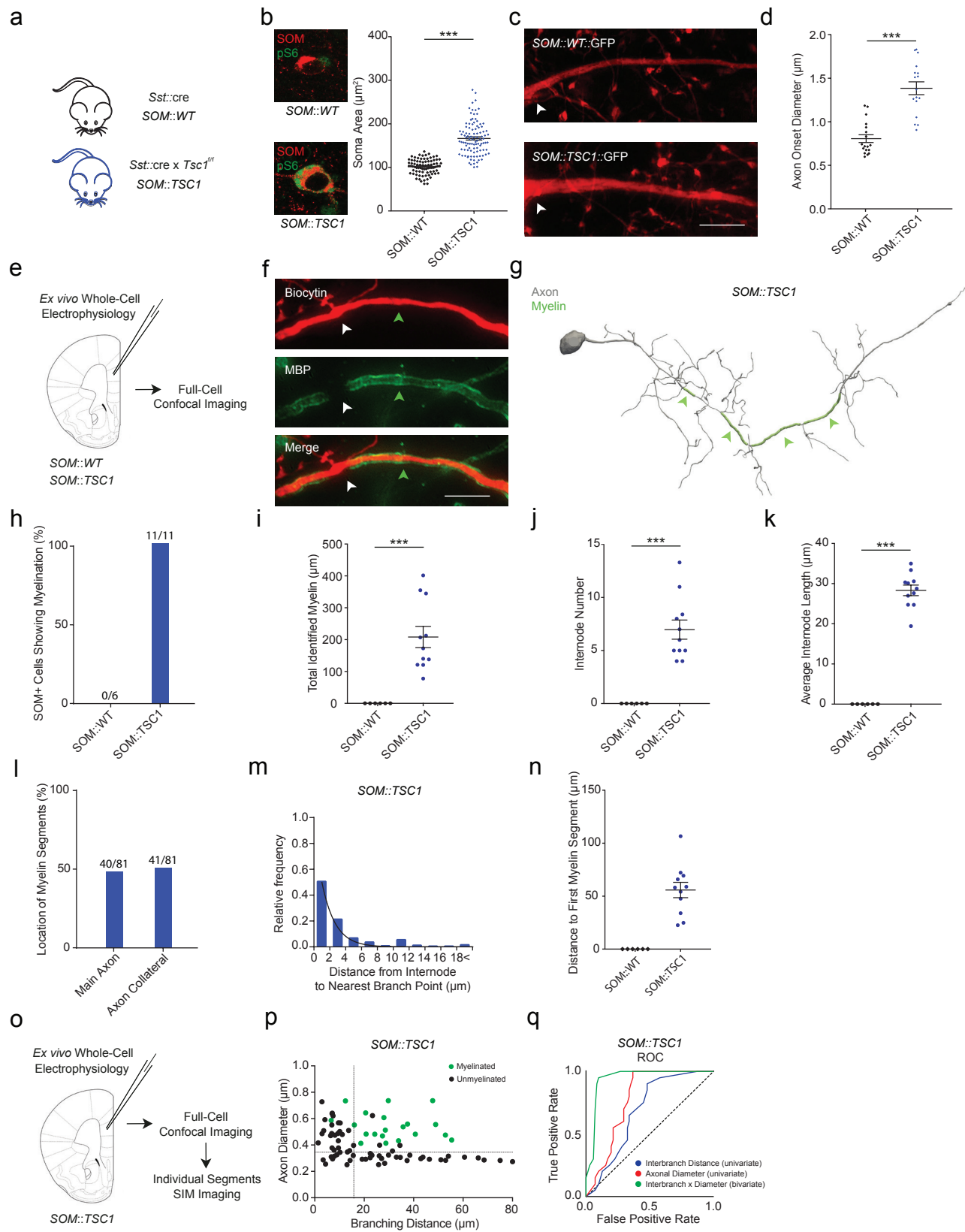


Figure 7 - Figure Supplement 1

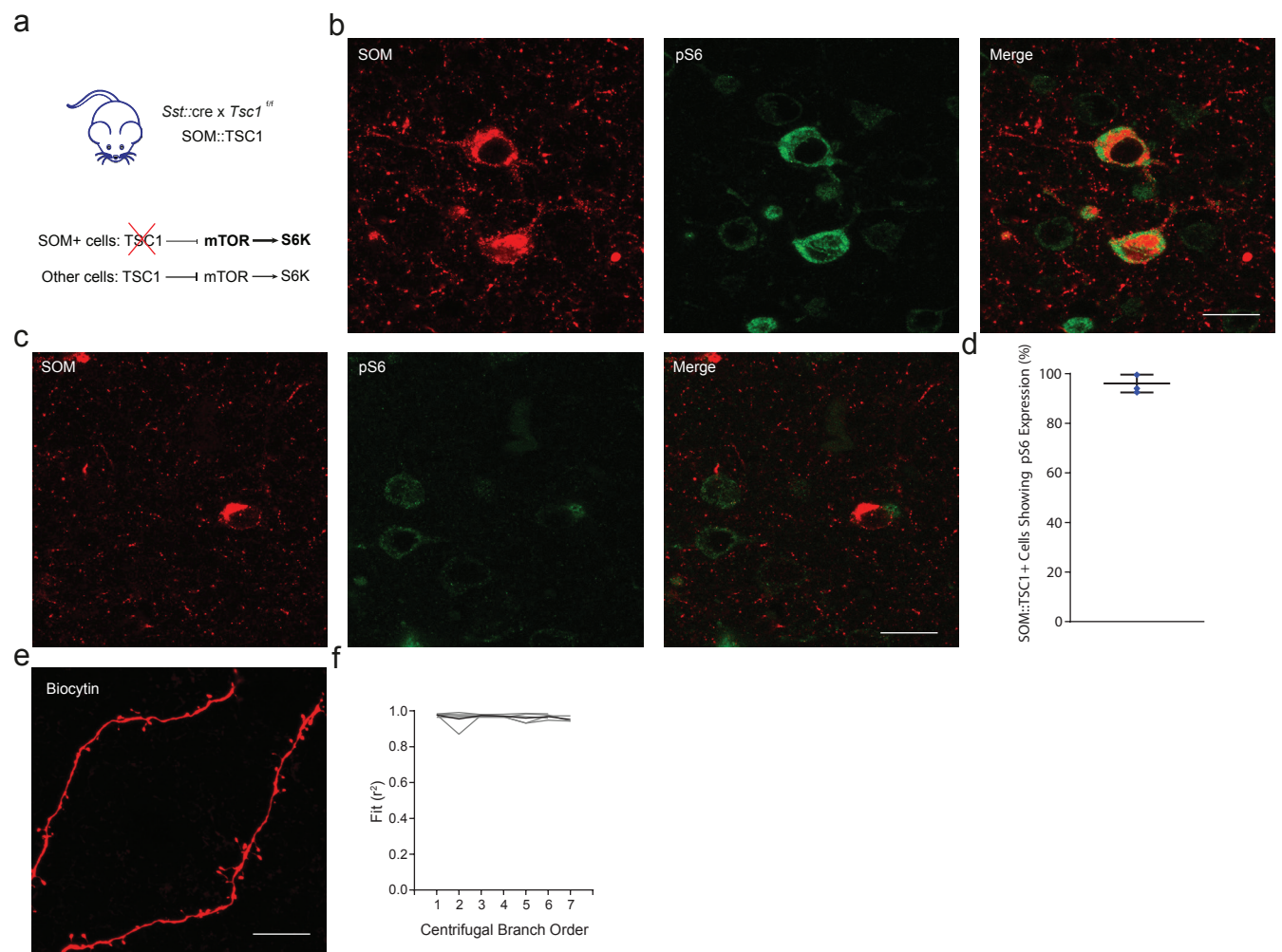


Figure 7 - Figure Supplement 2

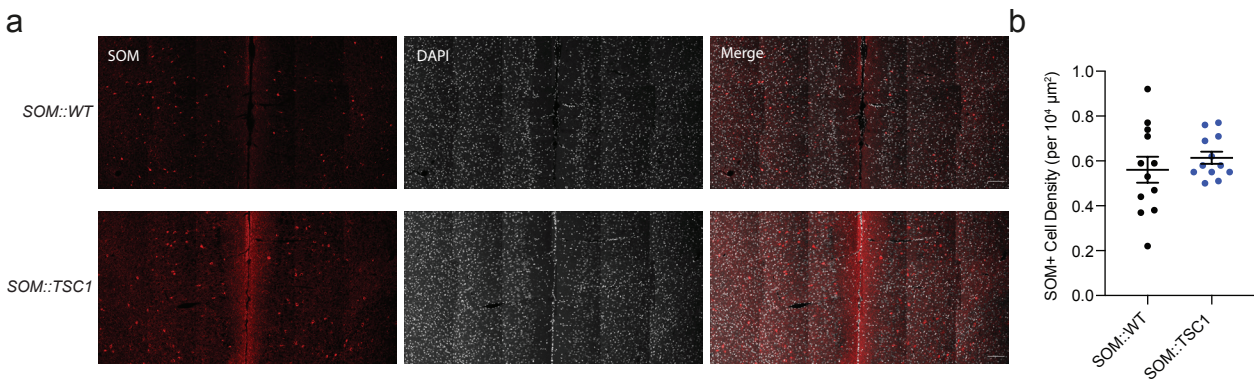


Figure 7 - Figure Supplement 3

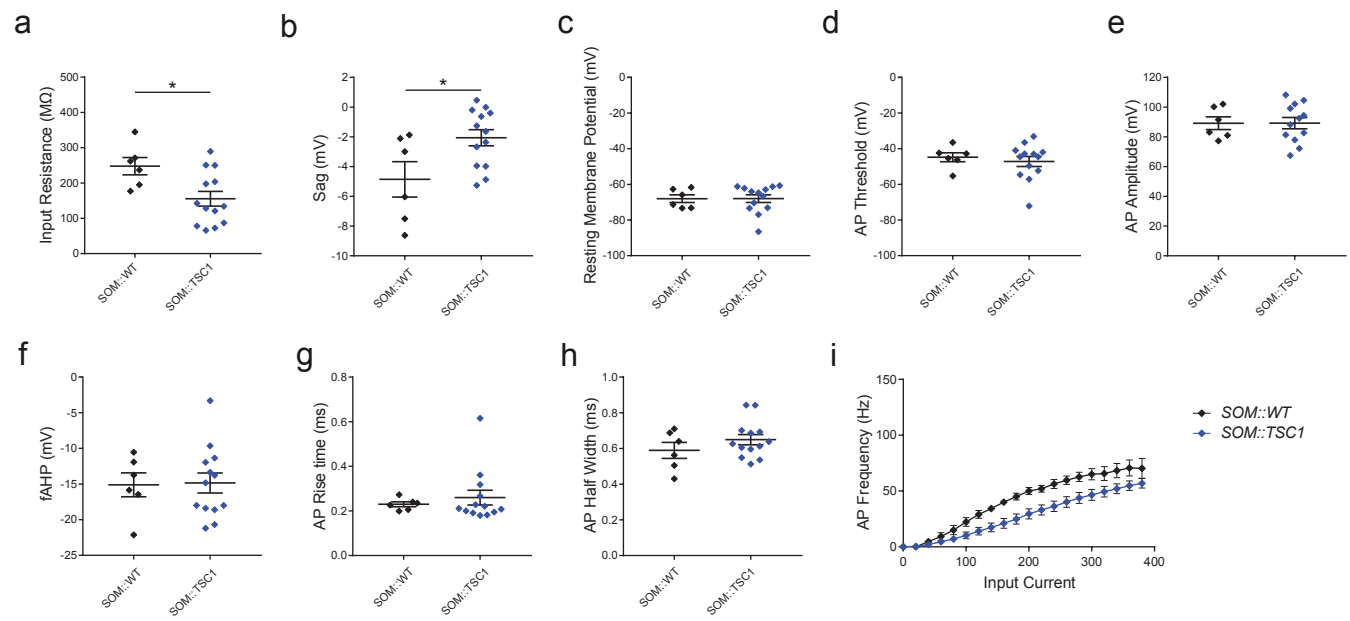




Figure 8

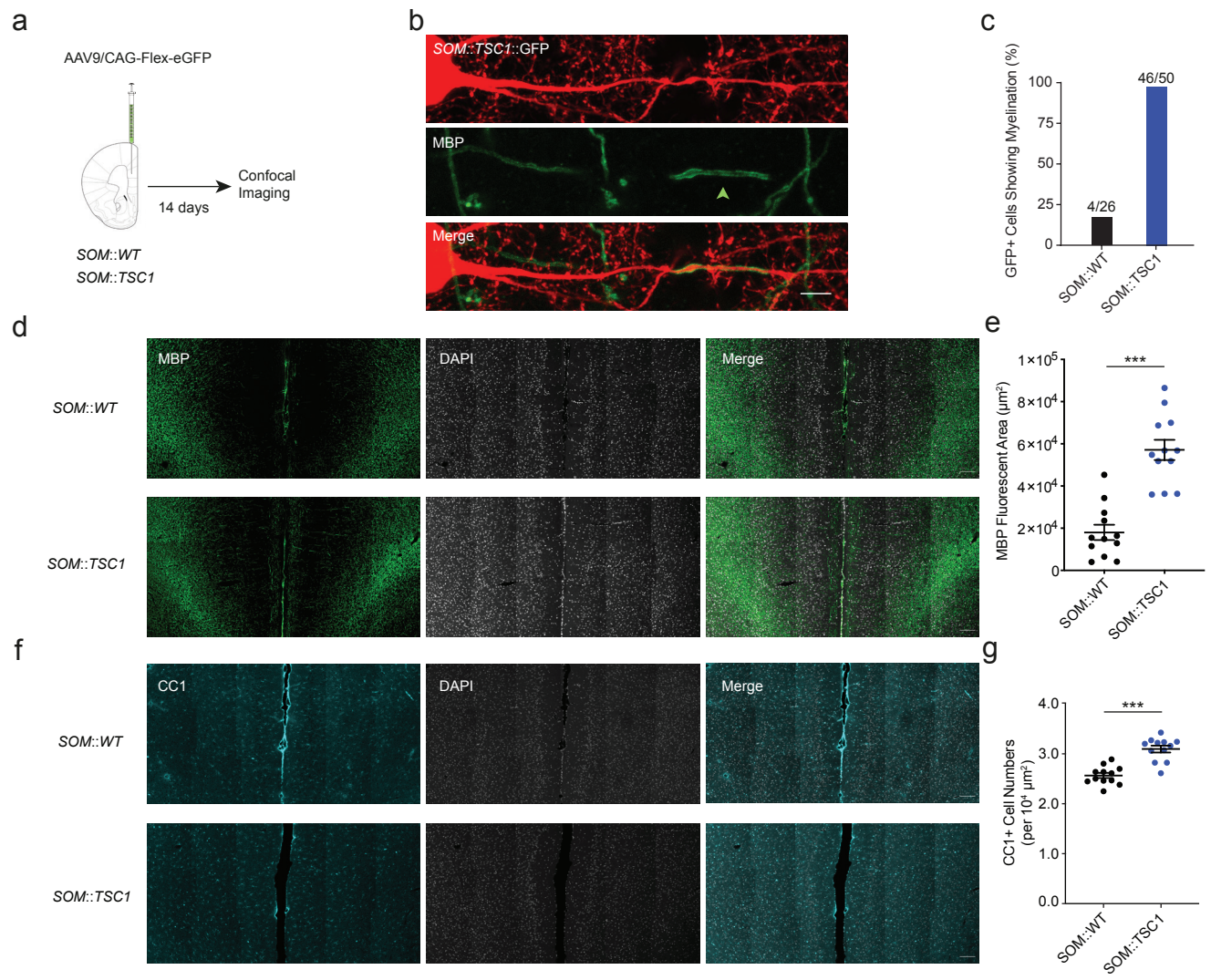


Figure 9

